Characterization of photoneutron fluxes emitted by electron accelerators in the 4 to 20 MeV range using Monte Carlo codes: a critical review

Adrien Sari

Université Paris-Saclay, CEA, List, F-91120 Palaiseau, France

*Corresponding author: Adrien Sari (e-mail address: adrien.sari@cea.fr)

Abstract

Applications of electron accelerators range from nuclear waste package assay and security-related tasks to radiation therapy. Some accelerator users are working with photoneutrons on purpose whereas their undesired effects affect some others. In any case, Monte Carlo codes are necessary to simulate the production of photoneutrons, characterize their fluxes, probe their impact or support interpretation of experimental data. In other words, studies aiming at characterizing photoneutron fluxes generated by electron accelerators typically require simulation work. In this paper, we critically review the performance of Monte Carlo codes to model photoneutron fluxes emitted by electron accelerators operating between 4 and 20 MeV, *i.e.* in the energy range of interest for such applications. First, we go through the state of the art and lay the foundations of current theoretical knowledge on photoneutrons. By carrying out additional investigations, we show that contamination of photoneutron fluxes by electroneutrons is likely to lie between 0 and 2%. Second, we assess the characteristics of photoneutron fluxes emitted by tungsten or tantalum conversion targets and by heavy water or beryllium secondary targets. This characterization step is conducted with MCNP6.2, which is one of the reference Monte Carlo codes, and built around three parameters, *i.e.* photoneutron yield cross-sections, energy and angular distributions. In particular, we demonstrate that erroneous parameters in the nuclear data of MCNP6.2 lead to (γ, xn) cross-section threshold errors for two tungsten isotopes, *i.e.* ^{182}W and ^{186}W, inducing in turn a global underestimation of photoneutron production in tungsten. Furthermore, by taking an in-depth look at nuclear data libraries, we show that photoneutron yield cross-sections are sometimes poorly

evaluated below 20 MeV, *e.g.* ^{2}H, ^{9}Be, ^{184}W. Third, thanks to vanadium and aluminium foils, we benchmark MCNP against photoneutron activation measurements conducted in the vicinity of three different electron accelerators, including a medical one. Simulation of these measurements denote a systematic underestimation trend extending from a few percent to a factor ten. Recent findings reported in the literature proved that photoneutron kinematics is implemented in MCNP with erroneous equations related to neutron inelastic scattering, causing hardening of photoneutron energy spectrum and may explain in part the discrepancies encountered in our MCNP benchmark study. Finally, in light of the three main sources of errors that potentially lead to unreliable results when simulating photoneutron fluxes – implementation of nuclear data and modelling of photonuclear physics in Monte Carlo codes as well as fundamental knowledge of photoneutron yield cross-sections – we issue recommendations for Monte Carlo code developers and users. Until further progress is made in the field of photoneutron simulation, mastering the current weaknesses of Monte Carlo codes could be the first milestone for their users.

Keywords: Linear electron accelerator (linac); Photonuclear reaction; Photoneutron; Electroneutron; Monte Carlo simulation; MCNP benchmark study

1. Introduction

When electrons hit a target made of heavy atomic nuclei, high-energy photons are created by *Bremsstrahlung*. In turn, photons can be converted to photoneutrons – *i.e.* neutrons produced by photonuclear reactions – if the photon energy is above the threshold of the reaction of interest. A thorough knowledge of the photoneutron fluxes generated by electron accelerators is of major importance for many applications, among which: radiation therapy, border security, and nuclear waste package characterization. In the frame of radiation therapy, high-energy photon beams delivered by medical accelerators are often used to deposit gamma doses locally on tumors. However, simultaneously, photoneutrons may lead to undesired neutron doses [1-5] deposited on the whole body of patients. In very different fields of applications, a linear electron accelerator (linac) enables to implement the photofission reaction – which is the basis of the active photon interrogation technique – in view of detecting Special Nuclear Material (SNM) such as uranium and plutonium isotopes either for cargo containers security checks [6, 7] or for nuclear waste packages characterization [8-11]. During active photon interrogation measurements, photoneutrons may represent spurious particles at the origin of unwanted neutron-induced fission reactions [12]. However, in view of enhancing characterization of nuclear waste packages, a linac can be at the center of a versatile platform enabling to perform either simultaneous active photon interrogation (photofission) and active neutron interrogation (fission) [13, 14] or non-simultaneous interrogations [15]. It should be nevertheless stressed that the second of these two methods enables to optimize both the high-energy photon and the photoneutron beams, and facilitates interpretation of results obtained with the two interrogation techniques. Moreover, a significant interest can also be reported towards linac-based neutron sources for a variety of applications such as: material analysis by neutron activation for different industrial applications [16, 17], Boron Neutron Capture Therapy (BNCT) [18], or applications related to nuclear reactors [19], among others. Furthermore, one would notice that such linac-based platforms also enable to deploy a third measurement technique – *i.e.* high-energy imaging – which provides useful and valuable information for the interpretation of results

obtained regarding, for instance: the analysis of a suspicious cargo container by photofission [7]; or the characterization of a nuclear waste package by active photon interrogation [20].

The electron-to-photon conversion targets of accelerators are usually made of tungsten or tantalum. It is worth to recall that the first characterization studies of photon beams and photoneutron fluxes emitted by such targets were conducted in the 1970's [21, 22]. The high-energy photon spectra produced by the *Bremsstrahlung* process due to electrons bombarding the target of an accelerator are continuous and have endpoints energies corresponding to the electron energy. Considering electron accelerators operated in the 4 to 20 MeV range, photoneutrons may be produced by different materials. Indeed, the energy thresholds of the (γ, n) reactions for ^{181}Ta or for the five isotopes of tungsten are roughly around 7 MeV, *i.e.* the neutron separation energy of the emitter nuclei. Therefore, if the electron energy is above this threshold, photoneutrons will be directly produced by the target of an electron accelerator. Moreover, if the electron energy is also above the (γ, 2n) reaction threshold, these reactions may also be brought into play and will contribute to the production of photoneutrons. Nevertheless, when the electron energies are close or below the (γ, n) reaction thresholds of the target materials, secondary targets including nuclei with lower (γ, n) energy thresholds can be used to achieve a significant photoneutron yield. The lowest energy threshold of the (γ, n) reaction is for ^{9}Be with a value of 1.67 MeV [23]. Another candidate would be deuterium (D or ^{2}H) with a (γ, n) reaction energy threshold at 2.22 MeV [23], which is more easily available in the chemical form of heavy water (deuterium oxide, D_2O). Secondary targets made of beryllium or heavy water have been commonly used with low energy electron accelerators operated as low as 4 MeV [24, 25]. However, as beryllium is toxic, a secondary target made of heavy water is often preferred, although tritium (T or ^{3}H) is potentially produced during the irradiation process. Considering x the neutron multiplicity equal to 1 or 2, Table 1 gathers weight percentages and energy thresholds of (γ, xn) reactions for each isotope [23] of the most common photon-to-neutron conversion targets found in electron accelerators operated in the 4 to 20 MeV range. For a given electron energy in this range, and depending on the use of one or two targets, their

compositions and dimensions, and on the settings of the accelerator, the photoneutron emission intensity begins around 10^7 and reaches 10^{11} neutrons per second in 4π sr [26-30].

(γ, xn) conversion target	Isotope	Weight percentage per isotope (%)	Energy threshold (MeV)	
			(γ, n) reaction	(γ, 2n) reaction
Heavy water	^{2}H	20	2.22	-
Beryllium	^{9}Be	100	1.67	20.56
Tantalum	^{181}Ta	99.99	7.58	14.22
Tungsten	^{180}W	0.12	8.41	15.35
	^{182}W	26.30	8.07	14.75
	^{183}W	14.28	6.19	14.26
	^{184}W	30.70	7.41	13.60
	^{186}W	28.60	7.19	12.95
Lead	^{206}Pb	24.10	8.09	14.82
	^{207}Pb	22.10	6.74	14.83
	^{208}Pb	52.40	7.37	14.11

Table 1. The most common photon-to-neutron conversion targets of electron accelerators operated in the 4 to 20 MeV range: weight percentages and energy thresholds of (γ, xn) reactions per isotope [23].

One would notice that data for ^{204}Pb, which represents 1.40% of the mass of natural lead, is not provided in Table 1 and in [23]. Nevertheless, it can be emphasized that lead – with a melting point at 327.5 °C – may not be the most common option for use as primary target of an electron accelerator. On another note, this material is often used to collimate photon beams and notably in medical accelerators. Thus, for electron accelerators devoted to radiation therapy, tungsten and lead usually account for most of the photoneutron emission [31, 32]. Moreover, while the contribution from the conversion target may be limited with such medical accelerators, the jaws of the accelerator may be at the origin of more than half of the photoneutron production (see Table IV and Fig. 10 of [32]). In the field of radiation therapy, neutron contamination from medical accelerators has been studied for many years [33, 34]. However, recent investigations have shown that the characterization of photoneutron fluxes emitted by accelerators is still a topic of major interest, and even at electron energies as low as 6 MeV [35]. It is also noteworthy to mention that the knowledge of the (γ, n) reaction energy thresholds may be discussed and that low (γ, n) energy threshold-elements could be found in small quantities both in the materials making up accelerators and in their surroundings. Whatever the field of application considered, Monte Carlo codes are widely used to simulate the production of photoneutrons from electron accelerators. Nevertheless, accuracy of results obtained may be the subject of questions and discussions.

In this paper, we investigate with a new eye the reliability of Monte Carlo codes to simulate photoneutron fluxes emitted by electron accelerators operating between 4 and 20 MeV. First, we review the state of the art and the current theoretical knowledge regarding photoneutrons. Photonuclear reactions will be described as well as emission of photoneutrons. The proportion of electroneutrons in photoneutron fluxes will be the subject of particular attention and additional estimates. Second, we evaluate the characteristics of photoneutron fluxes emitted either by tungsten or tantalum targets and then by heavy water or beryllium secondary targets. This characterization step will be conducted using MCNP6.2 [36, 37], which is one of the

Monte Carlo codes of reference and according to three main parameters, *i.e.* photoneutron yield cross-sections, energy spectrum and angular distribution. Third, we benchmark MCNP against neutron activation measurements conducted in the vicinity of three different electron accelerators, including a medical one. Finally, we will sum up the main sources of errors that potentially lead to unreliable simulated photoneutron fluxes, and make recommendations for Monte Carlo code developers as well as users who are working with photoneutrons on purpose or affected by their undesired effects, and most likely needing to simulate their production, characterize their fluxes, probe their impact or support interpretation of experimental data.

2. The physics of photoneutrons

2.1 Photonuclear reactions

In 1934, a pioneer experiment from J. Chadwick and M. Goldhaber showed that deuterium exposed to a radiothorium source emitting 2.6 MeV photons produces neutrons through the following reaction: ${}^{2}_{1}D + h\nu \rightarrow {}^{1}_{1}H + {}^{1}_{0}n$ [38]. Shortly after, L. Szilard and T. A. Chalmers observed that, under the influence of radium gamma-rays, neutrons are liberated from beryllium [39]. These findings will pave the way for a new field of research devoted to the study of interactions between photons and atomic nuclei, that is to say: photonuclear physics. Such interactions can lead to the emission of different types of photoparticles, among which neutrons and protons, respectively referred to as "photoneutrons" and "photoprotons". Nevertheless, it is important to underline that, in the photon energy range considered in this study (below 20 MeV), the number of photoprotons produced depends on the atomic mass number. Indeed, the probability that a charged particle succeeds in crossing the Coulomb barrier of a heavy nucleus is low [40]. This effect does not necessarily translate into higher energy thresholds for (γ, p) reactions than for (γ, n) reactions, as the two energy thresholds are rather close for heavy nuclei like ^{181}Ta or the five tungsten isotopes [23], but into a significant difference in their cross-section values. In other words, generation of photoprotons and other charged particles by electron accelerators in the 4 to 20 MeV range is negligible for the case of tantalum and tungsten targets and potentially significant when using light nuclei converters composed of deuterium or beryllium.

The total photonuclear cross-section per nucleon as a function of the photon energy is shown in Fig.1 [41]. For an incident photon energy of a few MeV and up to 20 MeV, the *Giant Dipole Resonance* (GDR) is the main mechanism responsible for the creation of photoneutrons. Thus, as in the framework of this paper we are interested in electron accelerators operated in the 4 to 20 MeV range, photoneutrons will mainly be produced by GDR. This model and a simple description of it was provided by M. Goldhaber and E. Teller in 1948 [42]. During this resonance, the incident photon interacts with the nucleus as a whole, with all neutrons and all protons moving in opposite directions within the nucleus (this motion is referred to as the "dipole vibration"). It is worth to highlight that for the case of actinides, *e.g.* isotopes of uranium and plutonium, GDR may lead to photon-induced fission of the nuclei (photofission), a reaction which was already predicted by N. Bohr and J. A. Wheeler in 1939 [43] and observed experimentally in the *Westinghouse Research Laboratories* in 1940 [44]. Years later [45], it was known that the GDR cross-section is characterized by a large peak at photon energies of approximately 20–23 MeV for light nuclei ($A \lesssim 40$) and 13–18 MeV for medium and heavy nuclei ($A \gtrsim 40$). For $A \gtrsim 40$, the energy of the peak can be approximated by $k_0 = 80\ A^{-\frac{1}{3}}$ MeV. The width of the GDR peak varies between approximately 3 MeV for heavy nuclei and 10 MeV for light nuclei.

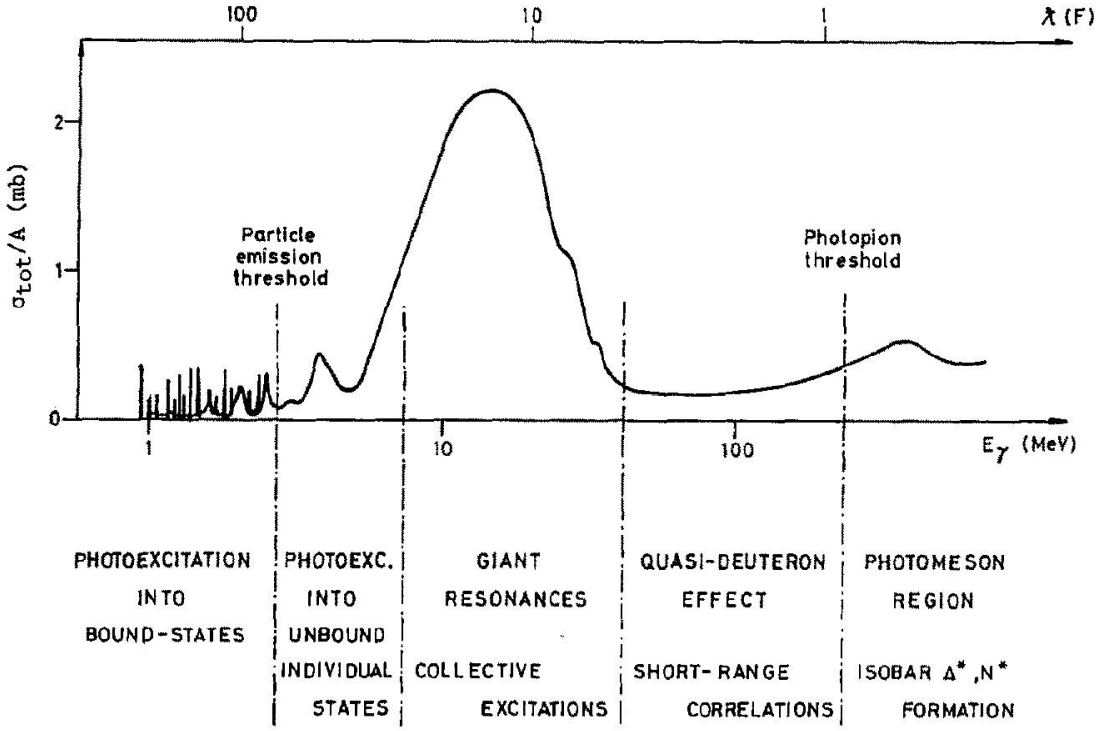

Fig. 1. Diagram of the total photonuclear cross-section per nucleon in mb as a function of the photon energy in MeV (primary x-axis) or its reduced wavelength in fm (secondary x-axis) [41].

2.2 Emission of photoneutrons

Photoneutrons created through the GDR may be emitted by two different processes. In 1937, V. F. Weisskopf introduced the *evaporation process* to describe the expulsion of particles from highly excited heavy nuclei [46]. In 1948, E. D. Courant and P. Jensen postulated the existence of a *direct emission process* in which the photon interacts directly with one of the particles in the nucleus without the formation of an intermediate "compound nucleus" state [40]. In 1956, D. H. Wilkinson described the “resonance direct” process by which a nucleon may be emitted from the nucleus in a single-particle state [47].

Photoneutrons emitted by evaporation process are foreseen to be characterized by an isotropic distribution [40]. Indeed, first, a collision between a photon of sufficient energy and a nucleus may lead to the formation of a compound nucleus in a well-defined state in which the incident energy is shared among all the constituents [46]. Second, the compound system disintegrates [46], which can be interpreted as if the memory

of the angle of the incident photon has been lost. However, the angular distribution of photoneutrons emitted by direct emission process should be in the form of $A + B\ \sin^2(\theta)$ [40], where θ is the angle between the incoming photon and the photoneutron produced. In other words, the direct emission of a photoneutron is expected to occur at 90° from the angle of the incident photon. In summary, E. D. Courant predicted in 1951 that the photoneutron spectrum will contain [40]:

- a predominant component composed of low energy photoneutrons produced by evaporation process, following a Maxwell distribution with a most probable energy of a few MeV and characterized by an isotropic angular distribution;
- a high-energy "tail" corresponding to photoneutrons produced by direct emission process, representing a few percents of all the photoneutrons emitted and characterized by an anisotropic angular distribution.

In 1960, F. Tagliabue and J. Goldemberg studied and compared the results from previous investigations conducted by numerous authors on the angular distribution of fast photoneutrons [48]. They reported that the experiments are difficult to compare due to the diversity of experimental conditions, and that one finds some discrepancies among the authors. They also performed measurements of angular distributions of photoneutrons produced by thirteen elements. They observed a maximum at 90° in the angular distribution measurements of fast photoneutrons produced by bismuth, lead and gold. In 1966, G. S. Mutchler reported in his doctoral thesis extensive experimental investigations on the angular distributions and energy spectra of photoneutrons from heavy elements [49]. He confirmed that the photoneutron spectra are characterized by an isotropic evaporation component, which dominates at low neutron energies, and an anisotropic resonance direct component, which dominates at high neutron energies. He also claimed that the transition from one component to the other is quite abrupt, typically taking place in a photoneutron energy interval of about one to two MeV. Moreover, he estimated the fraction of directly emitted photoneutrons – defined as the integral of the direct spectrum divided by the integral of the total spectrum – to be about 14% and approximately

constant with A, the mass number. Depending on the references and the radionuclides considered, the transition between the two photoneutron families, *i.e.* evaporation and direct emission, is essentially within the 3–5 MeV range of the total photoneutron energy spectrum.

The energy distribution of photoneutrons emitted by the evaporation process can be described by a Maxwell distribution [50] (page 368) [45] (page 71), in which T represents the "nuclear temperature", *i.e.* the temperature of the residual nucleus after emission

$$\left(\frac{dN_n}{dE}\right)_{evap} = \frac{E}{T^2} exp\left[-\frac{E}{T}\right] \quad (1)$$

In 1991, G. Tosi *et al.* proposed an approximation for the energy distribution of photoneutrons emitted by the direct emission process [51], in which E_{max} is the maximum energy of the *Bremsstrahlung* photon spectrum and S_n the neutron separation energy

$$\left(\frac{dN_n}{dE}\right)_{direct} = K \ln\left[\frac{E_{max}}{E + S_n}\right] \quad (2)$$

With K a normalization factor

$$K \int_0^{E_{max}-S_n} \ln\left[\frac{E_{max}}{E + S_n}\right] dE = 1 \quad (3)$$

Noting respectively α and β the proportions of evaporation and direct photoneutrons, the total energy distribution can be calculated

$$\left(\frac{dN_n}{dE}\right)_{total} = \alpha\left(\frac{dN_n}{dE}\right)_{evap} + \beta\left(\frac{dN_n}{dE}\right)_{direct} \quad (4)$$

Replacing the energy distributions of evaporation and direct photoneutrons by their expressions, the total energy distribution becomes

$$\left(\frac{dN_n}{dE}\right)_{total} = \alpha\left\{\frac{E}{T^2}exp\left[-\frac{E}{T}\right]\right\} + \beta\left\{K\ln\left[\frac{E_{max}}{E+S_n}\right]\right\} \quad (5)$$

Finally, replacing K by its expression, we find the total energy spectrum of photoneutrons derived by G. Tosi *et al.* [51]

$$\left(\frac{dN_n}{dE}\right)_{total} = \alpha\frac{E}{T^2}exp\left[-\frac{E}{T}\right] + \beta\frac{\ln\left[\frac{E_{max}}{E+S_n}\right]}{\int_0^{E_{max}-S_n}\ln\left[\frac{E_{max}}{E+S_n}\right]dE} \quad (6)$$

Eq. (6) can be computed and is plotted in Fig. 2 for the case of a tungsten target irradiated by 15 MeV electrons (distributions of evaporation and direct photoneutrons are also shown individually) taking into account:

- a nuclear temperature T of 0.5 MeV for tungsten nuclei, as originally deduced by R. F. Barrett *et al.* in 1973 [52] and which is in line with more recent investigations from T. von Egidy and D. Bucurescu [53];
- a neutron separation energy S_n of 7.35 MeV (average value calculated using the (γ, n) reaction energy thresholds provided in Table 1 for the five isotopes of tungsten and weighted by their abundancies);
- a maximum energy of the *Bremsstrahlung* photon spectrum E_{max} of 15 MeV;
- a fraction of direct photoneutrons β of 14%, as estimated by G. S. Mutchler [49], and thus a fraction of evaporation photoneutrons α of 86%;
- a derivation step of 1 keV.

In this example, the normalization factor K has a value of 0.416 MeV^{-1}. We can also highlight that: the total photoneutron energy spectrum is normalized to unit; the most probable energy is 0.5 MeV (which is in fact given by the "nuclear temperature"); the mean energy is about 1 MeV; and the transition area from evaporation to direct photoneutrons is around 3 MeV. It is also interesting to underline that Eq. (6) predicts that the higher the electron energy, the more energetic will be the direct photoneutrons produced by the electron accelerator. On another note, one should keep in mind that Eq. 6, based on approximations, is usually sufficient to describe the shape of the photoneutron energy spectra and the associated physical processes. However, the use of more sophisticated algorithms, such as the one proposed by J. C. Liu *et al.* in 1995-1997 [54, 55], would show a collapse of the direct photoneutron component in the range from 0 to ~2.5 MeV, which is in agreement with measurements from G. S. Mutchler [49].

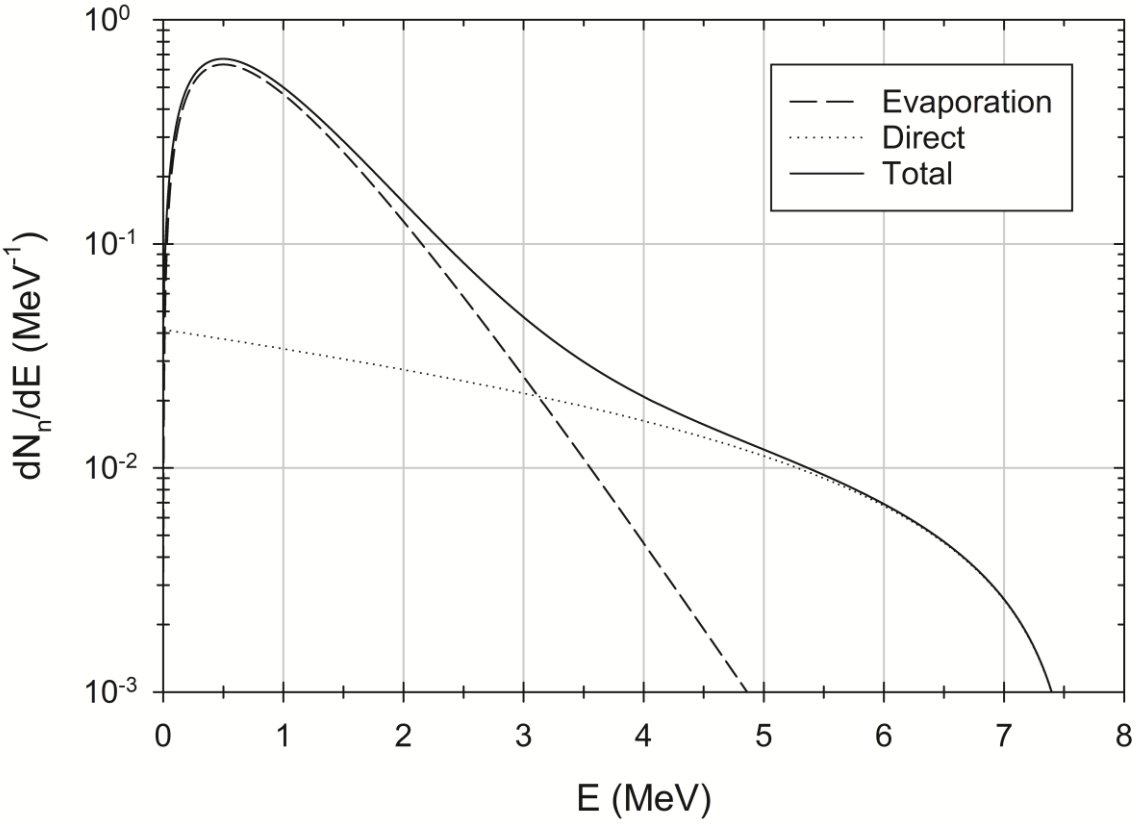

Fig. 2. Theoretical energy spectrum of photoneutrons emitted by a tungsten target irradiated by 15 MeV electrons (energy spectra of evaporation and knock-on photoneutrons are also plotted individually).

In summary, electron accelerators operated in the 4 to 20 MeV range generate two types of photoneutrons:

- *Boiled off photoneutrons* emitted by an evaporation process, of low energies, and for which an isotropic angular distribution is expected;
- *Knock-on photoneutrons* emitted by a direct emission process, of higher energies, and for which an anisotropic angular distribution is expected (with a privileged emission angle around 90° from the incident photon).

These fundamental characteristics enable to describe photoneutrons at the time of their emission on the scale of the atomic nucleus. From a macroscopic point of view, several characteristics and parameters of electron accelerators operated in the energy range studied may influence the energy spectra and angular distributions of the photoneutron fluxes produced. Indeed, it is likely that the anisotropic trend in the angular distribution of knock-on photoneutrons would be smoothed by two effects: the anisotropic angular distribution of the *Bremsstrahlung* photons; the shape, composition and density of the photoneutron-emitting material due to neutron scattering reactions. Furthermore, the isotropic trend of evaporation photoneutrons could also be remodeled by the geometry, composition and density of the photoneutron-emitting material. Regarding the energy of the photoneutron fluxes generated, tungsten or tantalum targets generally produce spectra characterized by a mean value of the order of 1 MeV. Nevertheless, when setups are implemented with a secondary target made of heavy water for instance (often consisting of a volume of several litres), photoneutrons emitted by deuterium nuclei could then be thermalized in the volume of the hydrogen-rich target, which could result in a lower mean energy of the photoneutron flux generated. Furthermore, in the case of medical accelerators – in which photoneutrons are produced by different parts of the machine (primary target, collimators, jaws, etc.) and potentially composed of various materials – both energy spectra and angular distributions of the photoneutron fluxes are foreseen to be impacted, with noticeable differences in comparison with the characteristics of photoneutrons at the time of their emission at the scale of the

nucleus. Therefore, whatever the type of electron accelerators used in the 4 to 20 MeV range, Monte Carlo transport codes are often necessary to characterize the photoneutron fluxes generated.

Regarding the physics of photoneutrons implemented in commonly used Monte Carlo simulation codes:

- Concerning the angular distribution, isotropy is often assumed in the GDR regime for simplicity [23];
- Concerning the energy spectrum, calculations in Monte Carlo codes may be done with different approaches. Information on the algorithms implemented in the codes are sometimes provided [56]. However, when it is not the case, thorough investigations are necessary and may bring to light errors in commonly used approximations, as explained by D.A. Fynan in 2020 [57].

2.3 Virtual photons and electroneutrons

In 1924, E. Fermi decomposed harmonically the electric field of a charged particle flying past an atom and compared it with the electric field of light with a proper frequency distribution [58]. He assumed that the probability of the atom being excited or ionised by the passing particle is equal to the probability of excitation or ionisation by the equivalent radiation. Among others, he applied this assumption to the excitation due to electrons. This approximation was taken up and developed by E. J. Williams and C. F. von Weizsäcker in 1933–1935 [59, 60] and is commonly referred to as the "equivalent photon approximation". Since incident electrons may produce *virtual photons* leading to electronuclear reactions, one might expect similarities between electronuclear and photonuclear reactions. Moreover, it should also be noticed that both (e, n) and (e, e'n) notations are used to refer to the electroneutron yield reactions, depending on if the outgoing electron can be detected or not during the reaction. In 1984, M. N. Martins *et al.* measured the (e, n) cross-section for ^{63}Cu from 13.5 to 60 MeV [61]. In 1987, E. Wolynec *et al.* measured the (e, n) cross-section for ^{181}Ta from 9 to 30 MeV [62]. In 1988, M. I. C. Cataldi *et al.* measured the electroneutron yield cross-section for ^{208}Pb, ^{209}Bi and ^{181}Ta from threshold to 22 MeV [63]. More recently in 2020, new measurements of electroneutron yield cross-sections for ^{181}Ta were reported but using a high-energy electron beam of 100 MeV [64], which

is above the energy range studied in this paper. Nowadays, the literature is not more furnished regarding the knowledge of such cross-sections. Nevertheless, it is interesting to notice that many authors report that the electroneutron yield cross-sections are about 137 times smaller than the photoneutron yield cross-sections. This ratio, originally stated in 1984 in the NCRP report No. 79 (page 16) [33], was unfortunately postulated without demonstration, and one would expect that the ratio between electronuclear and photonuclear cross-sections is not constant with the electron or photon energy.

In the electron energy range of interest in this paper, let us define the electronuclear yield cross-section

$$\sigma(e, xn) = \sigma(e, n) + 2\,\sigma(e, 2n)$$

and the photoneutron yield cross-section

$$\sigma(\gamma, xn) = \sigma(\gamma, n) + 2\,\sigma(\gamma, 2n)$$

in which the neutron multiplicities are included for both the (e, 2n) and (γ, 2n) reactions.

For the case of ^{181}Ta, the (γ, xn) cross-sections measured by Bergère *et al.* in 1968 [65] and the (e, xn) cross-sections measured by Cataldi *et al.* in 1988 [63] are plotted in Fig. 3. We evaluated the ratio between these cross-sections as a function of the photon or electron energy up to 20 MeV and results obtained are shown in Fig. 4. Overall, the contamination of the photoneutron fluxes by electroneutrons increases with the electron energy. More particularly, we can see that the emission of electroneutrons is roughly 1000 times less probable than the emission of photoneutrons at 10 MeV. This value turns out to be about 500 at 15 MeV and approximately 73 at 20 MeV. It is worth to emphasize that the value of 137 indicated in the NCRP report No. 79 [33] seems to only be appropriate for an energy close to 18 MeV. Moreover, as no (e, xn) cross-sections have ever been measured for any of the tungsten isotopes in the energy range of interest, we assume in first approach that the production of electroneutrons by tungsten is of the same order of magnitude as for ^{181}Ta.

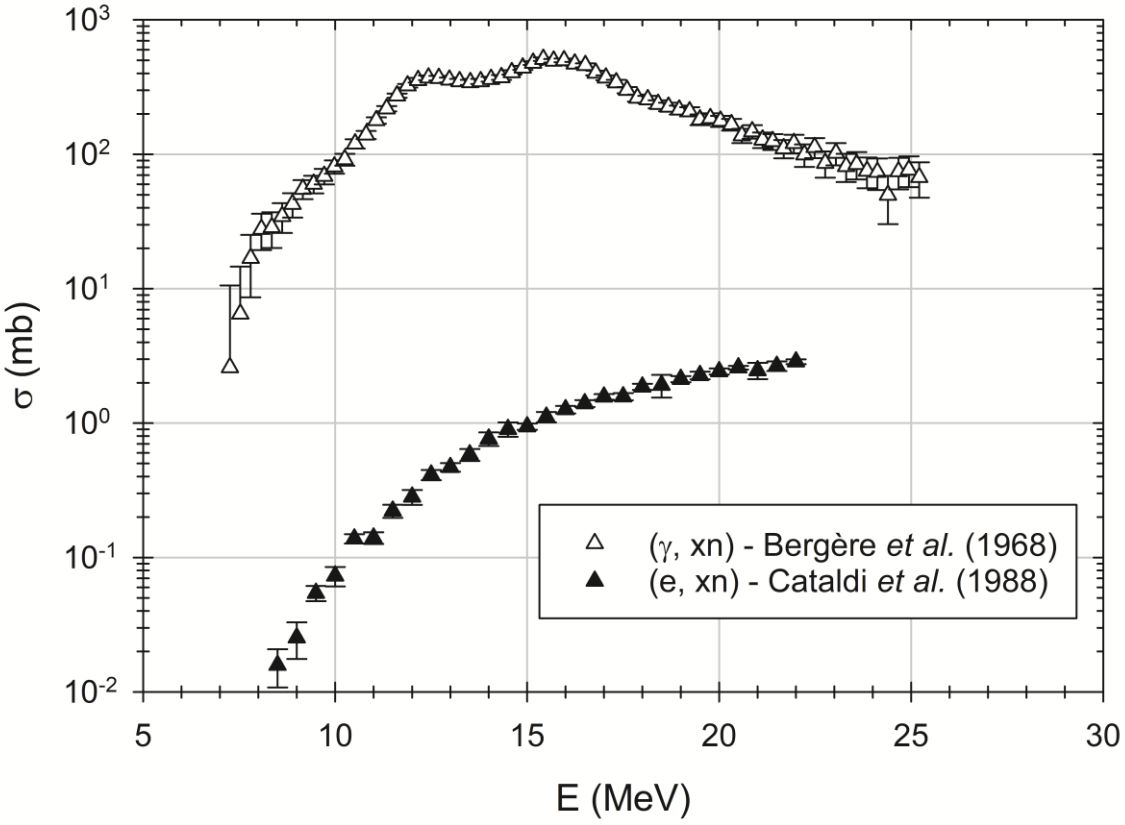

Fig. 3. Comparison of (γ, xn) [65] and (e, xn) [63] cross-sections for ^{181}Ta, as a function of the energy of the incident photon or electron.

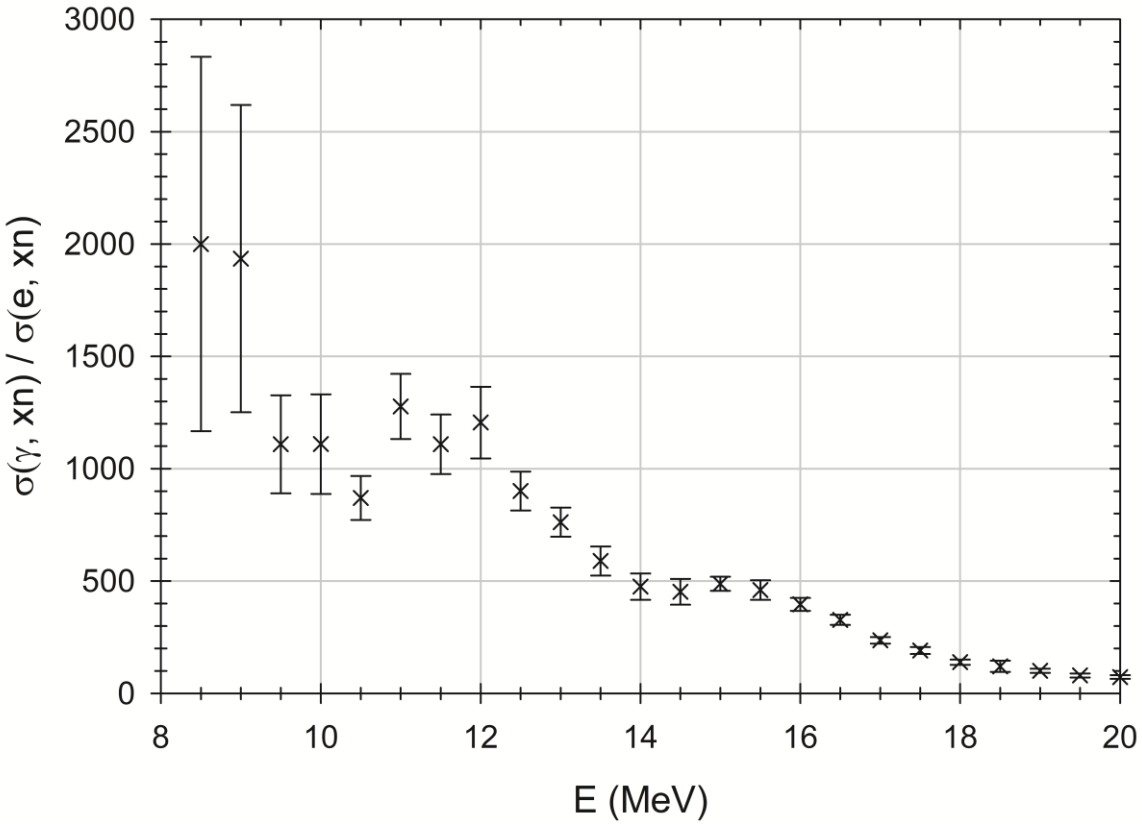

Fig. 4. Ratio between the (γ, xn) [65] and the (e, xn) [63] cross-sections for ^{181}Ta, as a function of the energy of the incident photon or electron.

Regarding the energy spectra and angular distributions of electroneutrons produced by electron accelerators in the 4 to 20 MeV range, little to no information exist. In 2011, in the absence of published data, K. Kosako *et al*. assumed that the angular distribution of electroneutrons was the same as that of *Bremsstrahlung* photons [66], which means that they expected electroneutrons to be emitted preferably in the forward direction with respect to the electron beam. They also assumed that the energy of electroneutrons was the same as the maximum energy of photoneutrons, which they presumed equal to 7 MeV for a copper target bombarded by 18 MeV electrons. However, these expected energy spectrum and angular distribution have not been demonstrated and were selected based on questionable assumptions. Therefore, until further fundamental experimental investigations are conducted, we would rather recommend assuming that electroneutron fluxes

are characterized by the same energy spectra and angular distributions as photoneutron fluxes (see section 2.2).

In 1975, V. M. Budnev *et al.* derived the equivalent photon approximation in expressions potentially applicable to the implementation of electronuclear reactions in Monte Carlo simulation codes [67]. At present, (e, n) or (e, e'n) electronuclear reactions are not implemented in most Monte Carlo transport codes, except for GEANT4 and FLUKA for instance [68]. Yet, we recommend using Monte Carlo simulation codes sparingly and with a high level of vigilance when aiming at simulating electroneutron fluxes produced by electron accelerators in the 4 to 20 MeV range. Indeed, knowledge on energy spectra and angular distributions, as well as validated electronuclear data and extensive Monte Carlo code benchmarking are all cruelly lacking to judge as reliable simulation results concerning electroneutron production from electron accelerators.

In any case, contamination of photoneutron fluxes by electroneutrons, when considering electron accelerators operated in the 4 to 20 MeV range and equipped with conversion targets, is expected to be limited. However, the emission of electroneutrons could become non-negligible when using electron accelerators in electron mode, *i.e.* without any conversion target, and potentially significant at high electron energies ($\gtrsim$ 30 MeV) at which the (e, xn) cross-sections may overtake the (γ, xn) cross-sections. Such a configuration without conversion target is notably encountered in the field of radiation therapy with medical accelerators operated in electron mode. The electroneutron production is foreseen to principally occur in the scattering foil, which is usually made of tungsten or tantalum and thick of a few tens of µm. In recent years, an increasing interest can be reported towards electroneutron production from medical accelerators [69-73]. In 2012, H.R. Vega-Carrillo and L.H. Pérez-Landeros measured the spectrum of electroneutrons in the vicinity of a 12 MeV medical accelerator (Varian 2100CD) using Bonner spheres [69]. They reported that the spectrum was mostly composed of thermal and epithermal neutrons, which is in fact explained by the moderation of electroneutrons in the irradiation hall. The measurement of the initial energy spectrum of electroneutrons from a fundamental point of view or in other words at the time of their emission would require an adapted

protocol and perhaps the use of a less complex geometry accelerator than the ones used in radiation therapy. In a broader scope of applications of electron accelerators, it is worth mentioning that V. T. Voronchev *et al.* claimed in 2005 to reach an intensity of 2×10^{13} n/s thanks to the $^{9}Be(e, e'n)^{8}Be$ reaction by inducing a 10 MeV electron beam on a dense beryllium plasma [74]. However, when coupling an electron accelerator operated in the 4 to 20 MeV range already equipped with a tungsten or tantalum target with a secondary target made of beryllium or heavy water, the production of electroneutrons is foreseen to be limited to the primary target. In other words, the production of electroneutrons in the beryllium or heavy water secondary target can be neglected.

In summary, the measurements of accurate fundamental data related to electroneutrons, such as: yield cross-sections, energy spectra and angular distributions; offer challenges that still have to be met as:

- it is not possible to detect and measure the energy of a virtual photon at the origin of the emission of an electroneutron;
- photoneutrons may also be produced along with electroneutrons, as electrons may undergo the *Bremsstrahlung* phenomenon and be responsible of the emission of photons that could in turn lead to the emission of photoneutrons;
- electroneutrons and photoneutrons are emitted simultaneously and could potentially have close (if not the same) characteristics in terms of energy spectra and angular distributions.

Finally, considering electron accelerators in the 4 to 20 MeV range equipped with electron-to-photon conversion targets, contamination of photoneutron fluxes by electroneutrons is likely to be overall below 2% and sometimes as low as 0.05% considering an accelerator operated at 9 MeV for instance.

3. Characterization of photoneutron fluxes by Monte Carlo simulation

3.1 Materials and methods

In section 3, we examine the characteristics of photoneutron fluxes emitted by electron accelerators in the 4 to 20 MeV range by Monte Carlo simulation using the MCNP code, which is developed by the *Los Alamos National Laboratory* (New Mexico, USA) and widely used by the scientific community working with electron accelerators. When new and complementary calculations are presented, the latter have been carried out using the latest version of the code, *i.e.* MCNP6.2 [36, 37] with nuclear data from the ENDF/B-VII.1 library [75]. In a first step, we characterize photoneutron fluxes emitted by tungsten or tantalum targets irradiated by electrons in the 7 to 20 MeV range. In a second step, we characterize photoneutron fluxes emitted by heavy water or beryllium secondary targets coupled with electron accelerators operated in the 4 to 9 MeV range. In any case, the photoneutron fluxes will be characterized according to three main parameters: the photoneutron yield cross-sections, energy distribution and angular distribution.

The MCNP code uses photoneutron yield cross-sections to simulate the production of photoneutrons. For verification purposes, we will extract the photoneutron yield cross-sections used by the code and compare them to cross-sections measured by different authors. It is important to highlight that according to this methodology the cross-sections extracted are the ones precisely used by the code and not the ones expected to be used and taken directly from the ENDF database. Let us describe the rate of a photonuclear reaction of interest,

$$R = \int_0^{E_{max}} \phi(E)\, N\, \sigma(E)\, dE$$

with:

- R, the photonuclear reaction rate of interest (in reactions/cm^3/s);
- $\phi(E)$, the photon flux (in photons/cm^2/s);
- N, the atomic density (in atoms/cm^3);

- $\sigma(E)$, the microscopic cross-section of the photonuclear reaction of interest (in cm^2).

The atomic density can be rewritten as,

$$N = \frac{\rho N_A}{M}$$

with:

- N, the atomic density (in atoms/cm^3);
- ρ, the material density (in g/cm^3);
- N_A, the Avogadro's constant ($\approx 6.022 \times 10^{23}$ atoms/mol);
- M, the atomic mass (in g/mol).

Finally, the microscopic cross-section of a photonuclear reaction of interest for a photon of energy E can be extracted using the following formula

$$\sigma(E) = \frac{R}{\phi(E) \times \frac{\rho N_A}{M}}$$

In MCNP, $\phi(E)$ can be calculated using an *F4 tally* and R can be calculated using an *F4 tally* coupled with an *FM4 card*, in which is specified the reaction of interest via a reaction type number (MT) either defined according to the ENDF-6 format manual [76] or the MCNP user's manual [77] for non-standard special reaction numbers. In the frame of this study, we will use:

- the sum of MT numbers from 50 to 91 to extract (γ, n) cross-sections (standard ENDF reaction numbers);
- the MT number 16 to extract (γ, 2n) cross-sections (standard ENDF reaction number);
- the MT number 1001 to extract (γ, Xn) cross-sections (non-standard special reaction number).

In order to determine the photoneutron energy and angular distributions, a sphere of one-metre radius is simulated with MCNP around the photoneutron-producing target. The photoneutron energy distribution can be determined thanks to the number of photoneutrons crossing the sphere per electron hitting the target, which will be calculated with an *F1 tally* and 10 keV energy bins indicated in an *E1 card*. The determination of the photoneutron angular distribution requests to set a 0° polar angle reference vector towards the electron direction, which can be done using the *FRV option* of an *FT card*. The *F1 tally* can then be coupled with 4° polar angle bins described in a *C1 card*. Furthermore, considering an $[\alpha, \beta]$ angular bin, α being the lower angle and β the upper one, each number of photoneutrons crossing the sphere in an $[\alpha, \beta]$ angular bin will be divided by $2\pi[\cos(\alpha) - \cos(\beta)]$ in order to normalize the latter number by steradian.

3.2 Characteristics of photoneutron fluxes emitted by tungsten or tantalum targets

3.2.1 Photoneutron yield cross-sections

In 2012, errors were discovered and reported in [78] regarding the (γ, xn) cross-sections used by the MCNPX code (version 2.7.B) [79] especially around the energy threshold of the (γ, xn) reactions for three of the five tungsten isotopes (^{182}W, ^{184}W and ^{186}W). These errors lead to an underestimation of the photoneutron production by tungsten and more particularly at low energy. By way of example, this underestimation of the photoneutron production by a tungsten target irradiated by 10 MeV electrons exceeds a factor of three [78]. Later on, these errors were identified in the frame of a collaboration with the development team of the TRIPOLI-4 Monte Carlo code [30] and explained by the fact that some photoneutron yields are set to zero instead of one at low energy in the nuclear data. In this paper, we will investigate if these errors in the (γ, xn) cross-sections for tungsten isotopes are still present in the latest version of the MCNP code, *i.e.* MCNP6.2 [36, 37].

However, before doing so, it is important to inform the reader that the photonuclear cross-sections from CNDC (Chinese Nuclear Data Centre) previously provided with MCNPX – in addition to the photonuclear data from ENDF – are no longer available with MCNP6.2. Furthermore, in order to circumvent the (γ, xn)

cross-sections errors at low energy in MCNPX, a potential solution was provided in [30] and consisted into calculating "manually" a (γ, xn) reaction rate thanks to the individual (γ, n) and (γ, 2n) reactions rates using the cross-sections from CNDC. Thus, this solution working with MCNPX becomes inapplicable with MCNP6.2.

Figs. 5 and 6 present the (γ, n), (γ, 2n) and (γ, xn) photonuclear cross-sections extracted from MCNP6.2 respectively for ^{180}W and ^{183}W. The (γ, xn) cross-sections are also reconstructed "manually" by summing the (γ, n) and (γ, 2n) cross-sections, including the neutron multiplicity. For both ^{180}W and ^{183}W, it is worth to notice that the (γ, xn) cross-sections are in excellent agreement with the (γ, n) + 2 (γ, 2n) manual reconstruction. It is important to highlight that, for these two isotopes, no experimental data are available [23] and a model was used to calculate these photonuclear cross-sections.

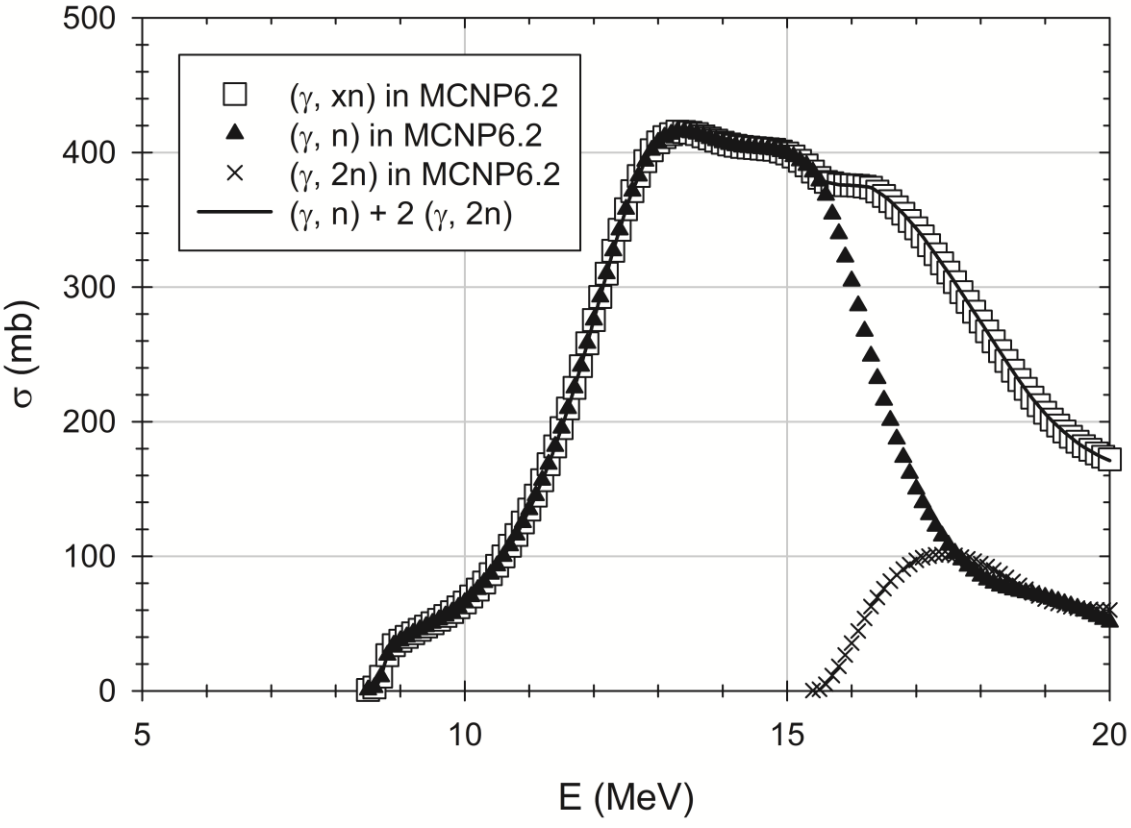

Fig. 5. Extraction of ^{180}W photonuclear cross-sections implemented in MCNP6.2.

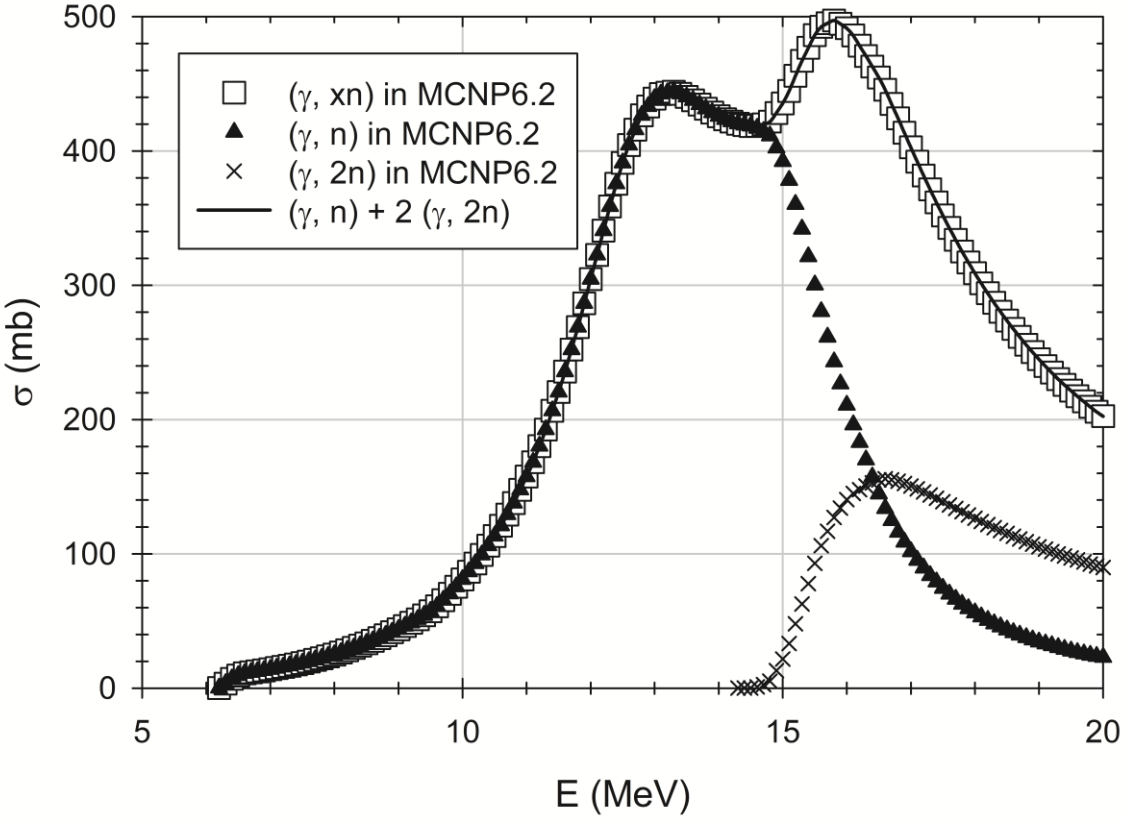

Fig. 6. Extraction of ^{183}W photonuclear cross-sections implemented in MCNP6.2.

The (γ, n), (γ, 2n) and (γ, xn) photonuclear cross-sections for ^{182}W extracted from MCNP6.2 are presented in Fig. 7. Two main comments can be made. First, the (γ, xn) cross-sections are in disagreement with the (γ, n) at low energy around the threshold. Second, the cross-sections measured by A. M. Goryachev and G. N. Zalesnyy in 1978 [80] enable to confirm that the erroneous cross-sections are the (γ, xn) ones. Fig. 8 presents the (γ, xn) photonuclear cross-sections for ^{184}W extracted from MCNP6.2. One would notice that the (γ, n) and (γ, 2n) cross-sections are not available for this isotope in MCNP6.2. The cross-sections measured by A. M. Goryachev *et al.* in 1973 [81], by A. Veyssière *et al.* in 1975 [82] and by A. M. Goryachev and G. N. Zalesnyy in 1978 [80] are in good agreement at low energy with the (γ, xn) cross-sections extracted from MCNP6.2. Nevertheless, the experimental data from Goryachev *et al.* (1973) suggest that the maximum of the (γ, xn) cross-sections curve around 15 MeV is undervalued, which could contribute to an underestimation of the photoneutron production by MCNP6.2 in the case of an electron accelerator equipped with a tungsten

target and operated above 14 MeV. While the first problem brought to light involved errors in the nuclear data of the MCNPX and MCNP6.2 codes, this second problem is different and relates to the lack of fundamental knowledge of photonuclear cross-sections. The (γ, n), (γ, 2n) and (γ, xn) photonuclear cross-sections for ^{186}W extracted from MCNP6.2 are presented in Fig. 9. The two comments previously made for ^{182}W are also relevant for ^{186}W. First, the (γ, xn) cross-sections are in disagreement with the (γ, n) at low energy around the threshold. Second, the cross-sections measured by B. L. Berman *et al.* in 1969 [83], by A.M. Goryachev *et al.* in 1973 [81] and by A. M. Goryachev and G. N. Zalesnyy in 1978 [80] enable to confirm once again that the erroneous cross-sections are the (γ, xn) ones. In other words, the (γ, xn) cross-sections threshold errors for ^{182}W and ^{186}W present in MCNPX and discovered in 2012 [78] when using the ENDF library are unfortunately still relevant in MCNP6.2 in 2022.

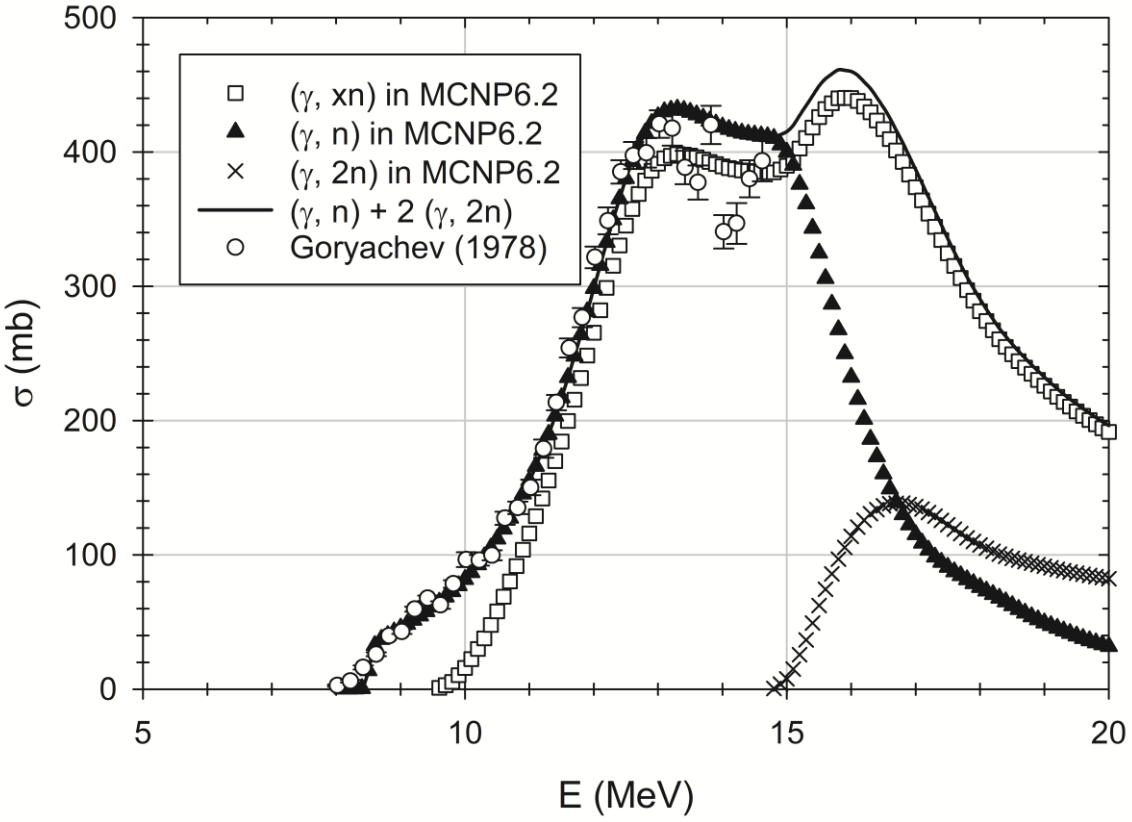

Fig. 7. Extraction of ^{182}W photonuclear cross-sections implemented in MCNP6.2 and comparison with experimental data.

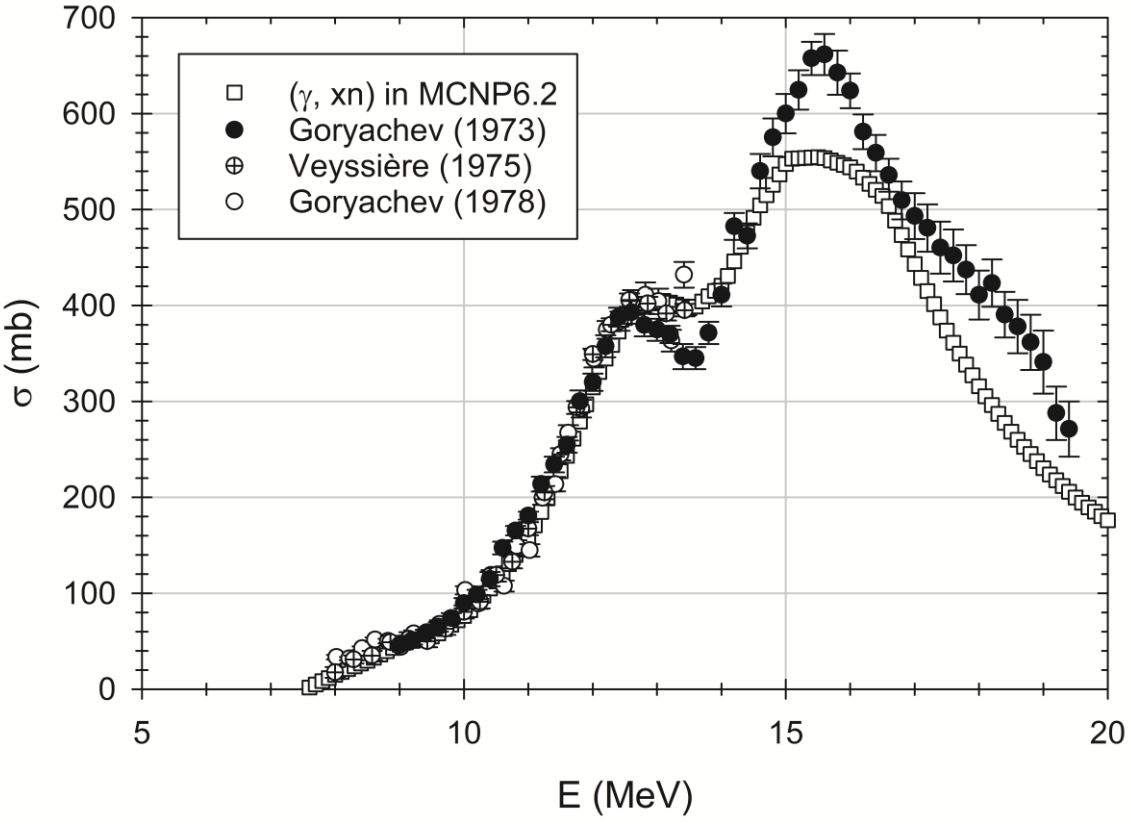

Fig. 8. Extraction of ^{184}W photonuclear cross-sections implemented in MCNP6.2 and comparison with experimental data.

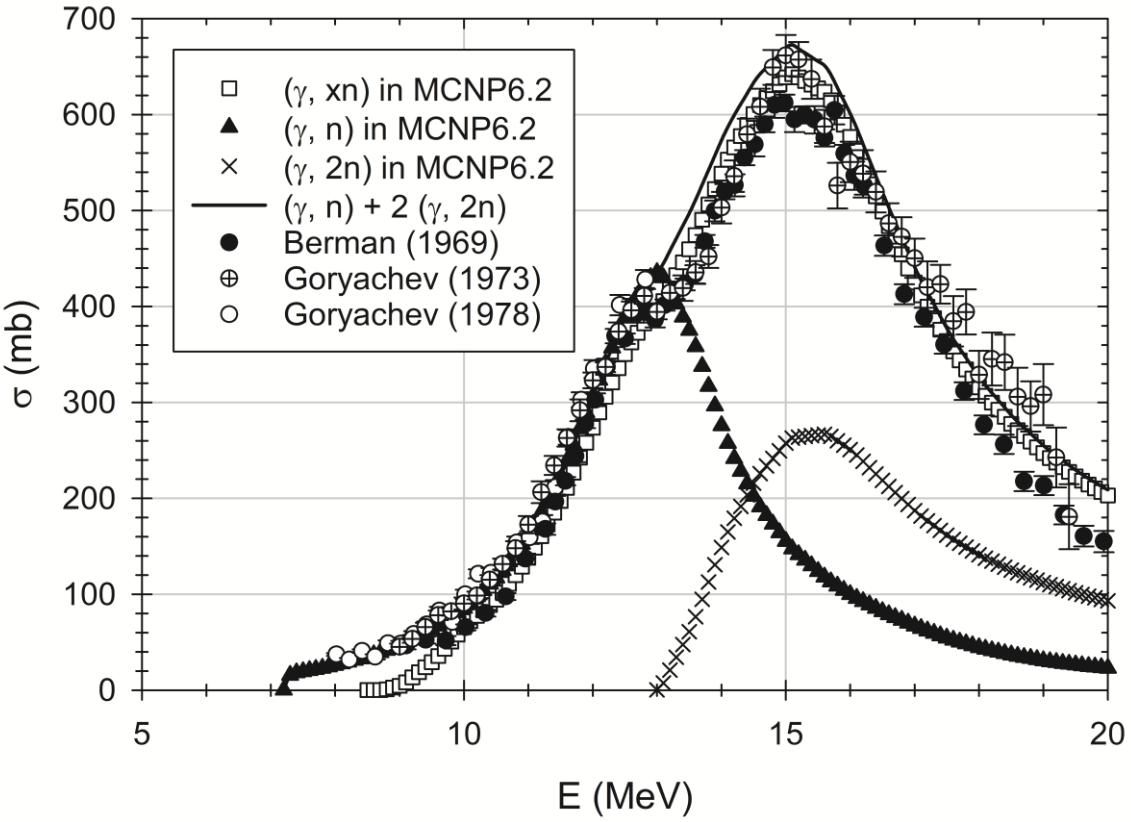

Fig. 9. Extraction of ^{186}W photonuclear cross-sections implemented in MCNP6.2 and comparison with experimental data.

In order to assess the impact of the (γ, xn) cross-sections threshold errors for ^{182}W and ^{186}W on the photoneutron production in the case of a tungsten target simulated with MCNP6.2, first, we calculated the (γ, xn) reaction rate in a target made of natural tungsten, which is composed of the five tungsten isotopes with their relative abundancies. Second, we simulated individually five targets each one being composed at 100% of one of the isotope of tungsten. For the targets made of either ^{180}W, ^{183}W or ^{184}W, we calculated directly the (γ, xn) reaction rates in the targets, whereas for the targets made of either ^{182}W or ^{186}W, and in order to avoid the (γ, xn) cross-sections threshold errors, we calculated "manually" the (γ, xn) reaction rate in the target by summing a (γ, n) and two (γ, 2n) reaction rates. Third, the "corrected" (γ, xn) yield was obtained by summing according to their relative abundancies the "non-erroneous" (γ, xn) reaction rates

obtained in the five individual targets. This comparison was conducted 14 times for electron energies from 7 to 20 MeV by 1 MeV steps. The results obtained for a 5 mm-thick target are gathered in Table 2. At 7 MeV, the (γ, xn) and the "corrected" yields match perfectly as at this energy the only isotope contributing to the photoneutron production is ^{183}W. At 10 MeV, the underestimation of the photoneutron production due to the (γ, xn) threshold errors for ^{182}W and ^{186}W in MCNP6.2 reaches nearly a factor of two. Above 15 MeV, the underestimation is below 20 %. It is important to highlight that the ratios provided in Table 2 may also be used by the reader as scaling factors in view of reevaluating photoneutron yields from tungsten targets irradiated by electrons in the 7 to 20 MeV range, which are underestimated in MCNP6.2.

Electron energy (MeV)	$\frac{(\gamma, xn)\ yield}{corrected\ \ yield}$
7	1.00
8	0.69
9	0.56
10	0.53
11	0.58
12	0.66
13	0.74
14	0.75
15	0.83
16	0.86
17	0.87
18	0.89
19	0.90
20	0.90

Table 2. Photoneutron yields emitted by a tungsten target irradiated by mono-energetic electrons in the 7 to 20 MeV range: ratios between the photoneutron yields calculated with MCNP6's erroneous (γ, xn) cross-sections and calculated according to the methodology proposed in this paper to avoid the (γ, xn) cross-sections threshold errors.

In order to avoid the errors encountered with a tungsten target regarding the production of photoneutrons with the MCNP code, one could be tempted to use a tantalum target instead. Fig. 10 presents the (γ, xn) photonuclear cross-sections for ^{181}Ta extracted from MCNP6.2. One would also notice that the (γ, n) and (γ, 2n) cross-sections are not available for this isotope in MCNP6.2. The cross-sections measured by R. Bergère *et al.* in 1968 [65] are roughly in agreement with the (γ, xn) cross-sections extracted from MCNP6.2 at both low energy and around the maximum of the (γ, xn) cross-sections curve around 16 MeV. Nevertheless, few experimental data exist concerning the photonuclear cross-sections for ^{181}Ta and the use of a tungsten conversion target is the most common industrial solution chosen by electron accelerator manufacturers.

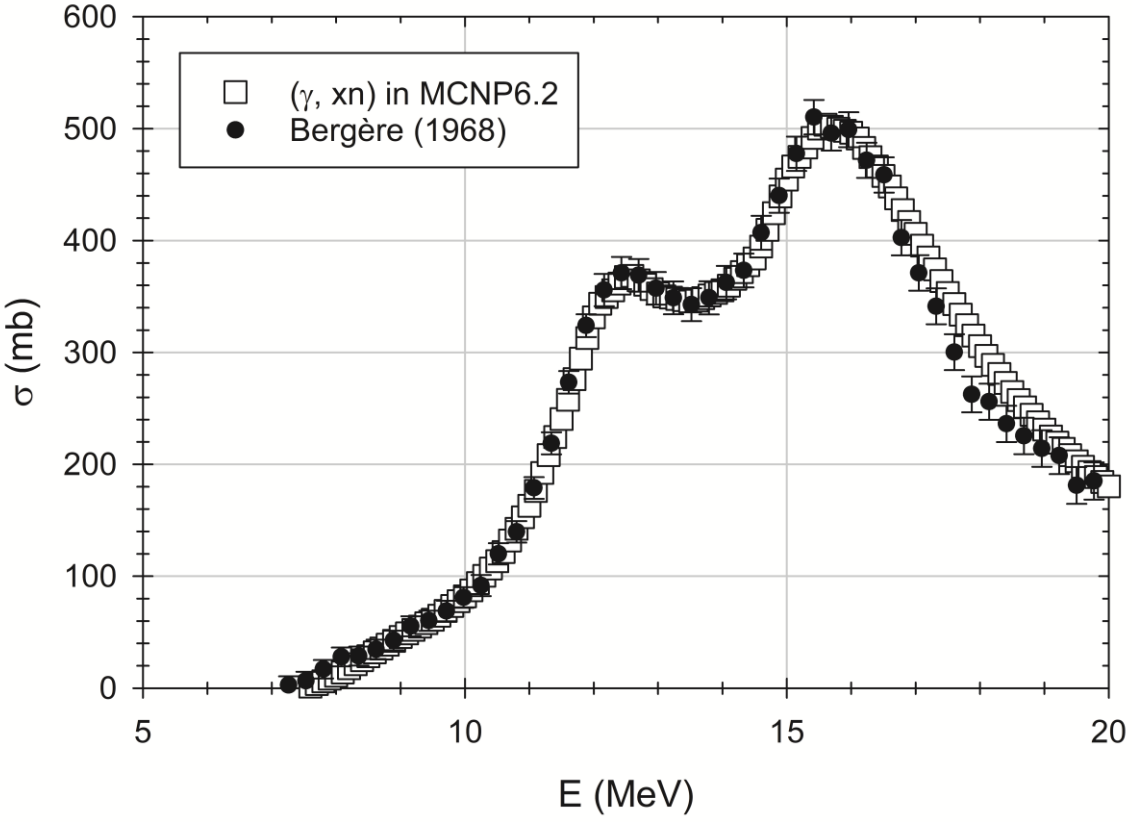

Fig. 10. Extraction of ^{181}Ta photonuclear cross-sections implemented in MCNP6.2 and comparison with experimental data.

3.2.2 Energy distribution

We simulated with MCNP6.2 the energy distributions of the photoneutron fluxes emitted by both tungsten and tantalum targets irradiated by 15 MeV electrons (mono-energetic source). Fig. 11 presents the results obtained. As discussed in section 2.2, the photoneutron energy spectrum is foreseen to follow a Maxwell-Boltzmann curve. Nevertheless, the shape of the energy distribution obtained for the case of a tantalum target below 0.5 MeV is not typical of such a Maxwell-Boltzmann curve, which was already observed using the MCNPX code in 2013 [30]. Fig. 12 shows the energy distributions of the photoneutron flux emitted by a tantalum target irradiated by 9 to 18 MeV electrons by 3 MeV steps, simulated with MCNP6.2. The strange shape of the energy spectrum obtained for a tantalum target under 0.5 MeV appears to be present whatever

the electron energy. It is likely that this shape does not have any physical interpretation, and could be due to inaccurate algorithms dedicated to the photoneutron production in the MCNP code.

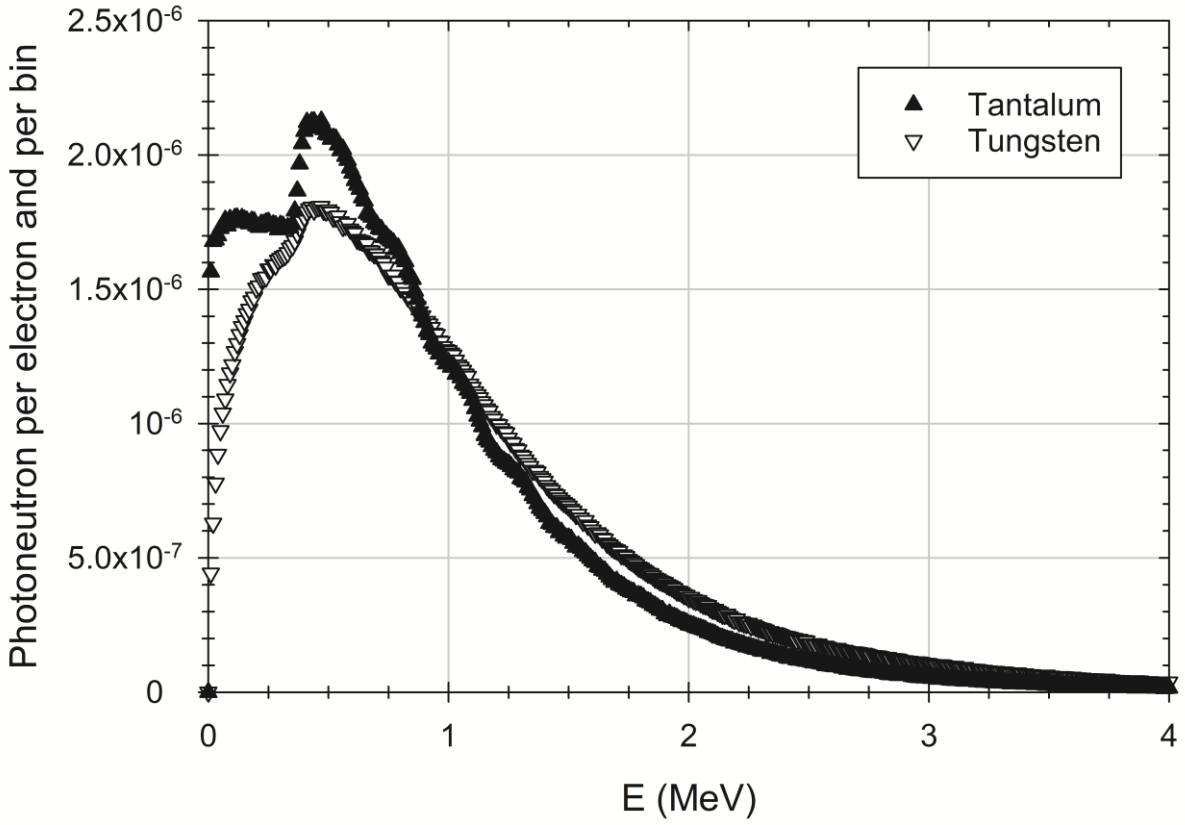

Fig. 11. Energy distributions of the photoneutron fluxes emitted by a tungsten or a tantalum target irradiated by 15 MeV electrons, simulated with MCNP6.2.

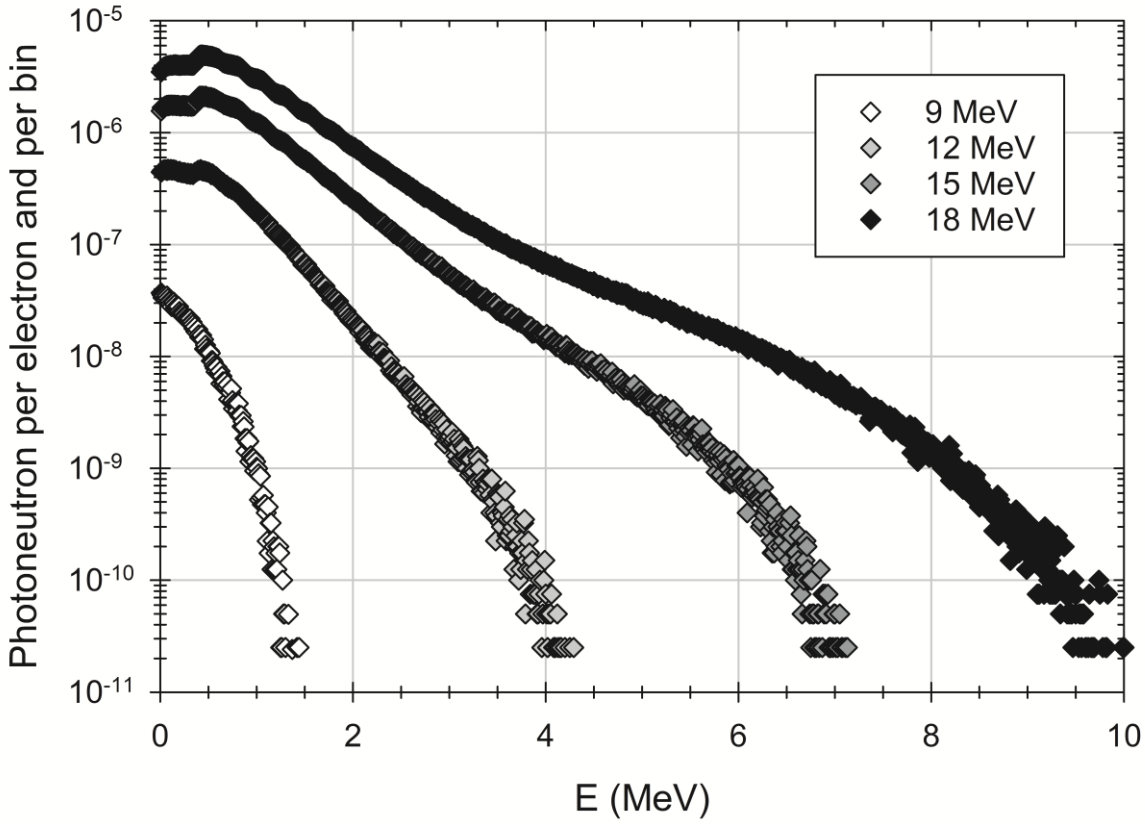

Fig. 12. Energy distributions of the photoneutron fluxes emitted by a tantalum target irradiated by either 9, 12, 15 or 18 MeV electrons, simulated with MCNP6.2.

3.2.3 Angular distribution

We also simulated with MCNP6.2 the angular distributions of the photoneutron fluxes emitted by both tungsten and tantalum targets irradiated by 15 MeV electrons. The target thickness is 5 mm and the diameter 5 cm. Fig. 13 presents the results obtained. Two comments can be made. First, the two energy spectra overlap each other. Second, a gap appears at 90°, along the diameter of the target. Fig. 14 shows the angular distributions of the photoneutron fluxes emitted by tungsten targets of 5 mm of thickness and either 5 mm or 5 cm of diameter irradiated by 15 MeV electrons, simulated with MCNP6.2. The angular distribution obtained for a target of 5 mm of diameter is isotropic, thereby proving that the gap observed at 90° for the case of a target of 5 cm of diameter is due to target geometry effects. As discussed in section 2.2, knock-on photoneutrons emitted by a direct emission process are expected to be present in the photoneutron energy distribution above a few MeV and characterized by an anisotropic angular distribution, with a privileged emission angle around 90° from the incident photon. Fig. 15 presents the normalized angular distributions of the photoneutron flux components from 0 to 5 MeV and from 5 to 20 MeV, emitted by a 5 mm-diameter tungsten target irradiated by 15 MeV electrons, simulated with MCNP6.2. The photoneutron component with an energy from 5 to 20 MeV appears to be isotropic as well as the 0 to 5 MeV component. We can infer from these results that the MCNP code does not simulate the direct component of photoneutron fluxes.

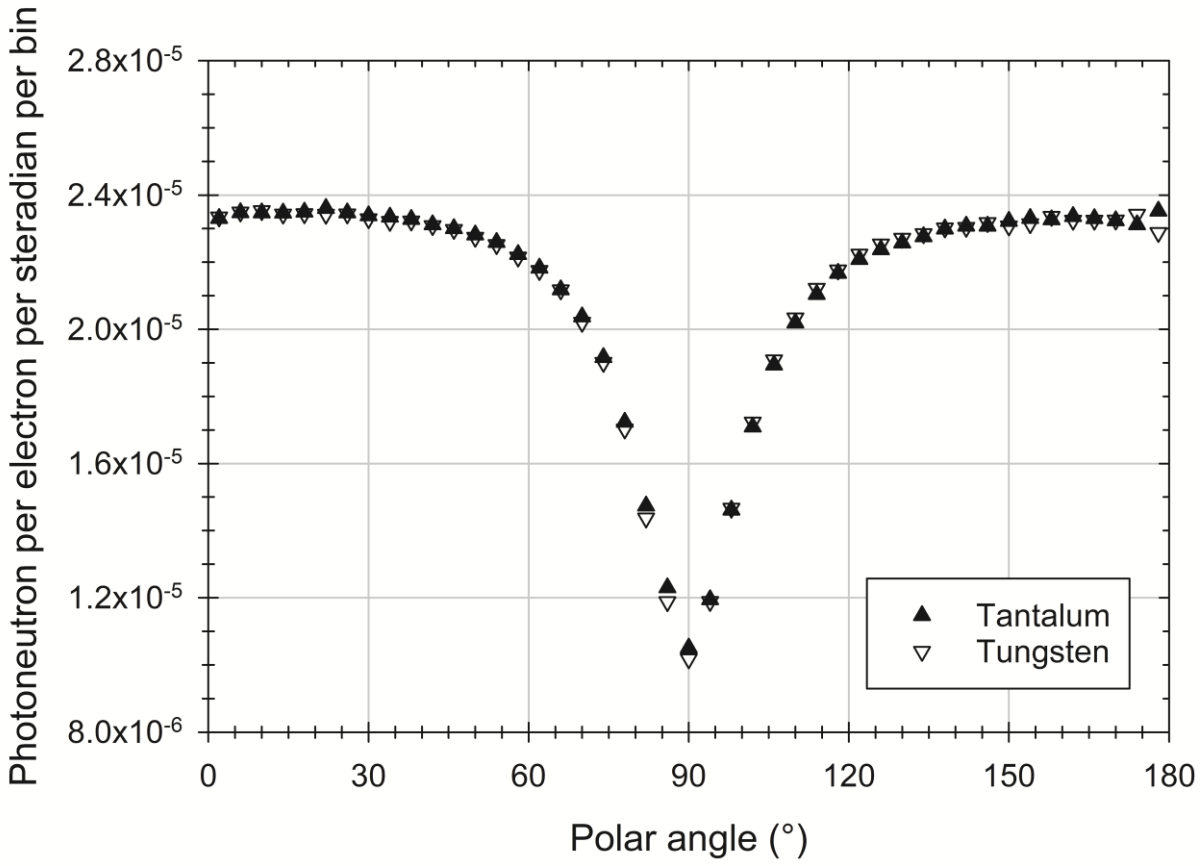

Fig. 13. Angular distributions of the photoneutron fluxes emitted by tantalum and tungsten targets of 5 mm of thickness and 5 cm of diameter irradiated by 15 MeV electrons, simulated with MCNP6.2.

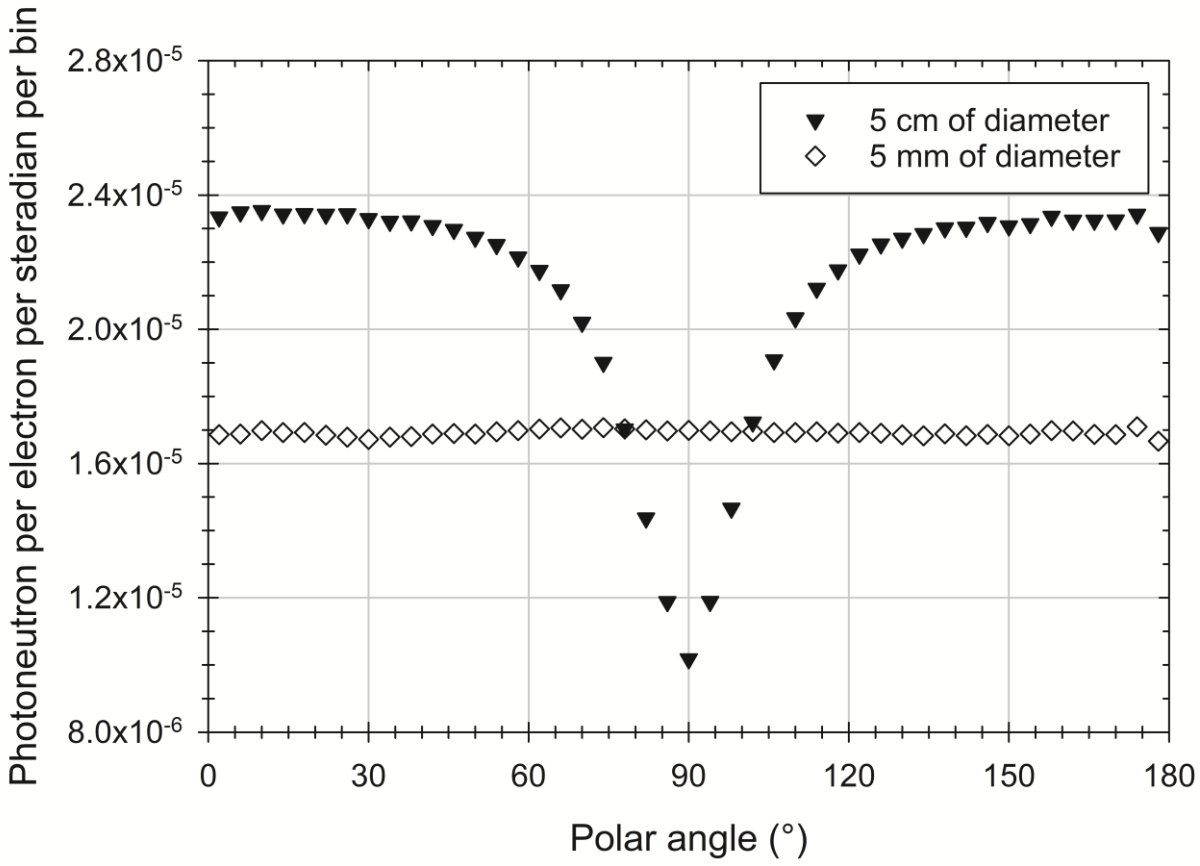

Fig. 14. Angular distributions of the photoneutron fluxes emitted by tungsten targets of 5 mm of thickness and either 5 mm or 5 cm of diameter irradiated by 15 MeV electrons, simulated with MCNP6.2.

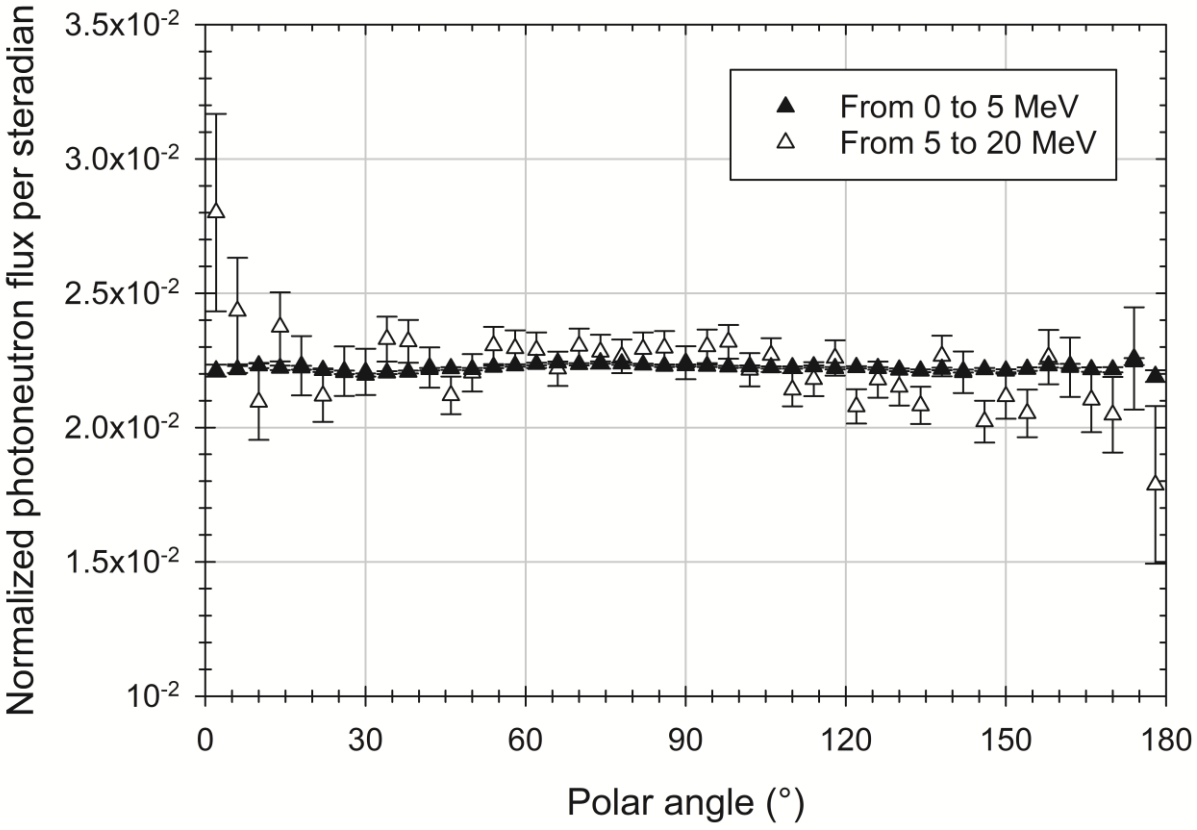

Fig. 15. Normalized angular distributions of the photoneutron flux components from 0 to 5 MeV and from 5 to 20 MeV, emitted by a 5 mm-diameter tungsten target irradiated by 15 MeV electrons, simulated with MCNP6.2.

3.3 Characteristics of photoneutron fluxes emitted by heavy water or beryllium secondary targets

3.3.1 Photoneutron yield cross-sections

As a reminder from section 1, a heavy water secondary target enables to produce photoneutrons through (γ, n) reactions on the deuterium nuclei contained in the latter. Obviously, in the case of a heavy water secondary target, (γ, 2n) reactions are prohibited as deuterium (^{2}H) is composed of a single neutron. The (γ, n) photonuclear cross-sections for ^{2}H extracted from MCNP6.2 are presented in Fig. 16. Experimental data measured by J. Ahrens in 1974 [84], by Y. Birenbaum in 1985 [85], by K. Y. Hara in 2003 [86] and the data from the IAEA/PD-2019 library [87] are also plotted on this graph. We can deduct from this figure that the maximum of the (γ, n) cross-sections curve around 4.5 MeV is undervalued. In other words, the photoneutron flux emitted by a heavy water target coupled with an electron accelerator operated in the 4 to 9 MeV range is likely to be underestimated when simulated with the MCNP code.

The (γ, xn) photonuclear cross-sections for ^{9}Be extracted from MCNP6.2 are presented in Fig. 17. Experimental data measured by U. Kneissl in 1975 [88], by H. Utsunomiya in 2015 [89], and the data from the JENDL/PD-2004 library [90] are also plotted on this graph. This figure brings to light significant disagreements between the (γ, xn) cross-sections implemented in MCNP6.2 and especially with both the measurements from H. Utsunomiya and the data from the JENDL library. We therefore recommend conducting MCNP simulations involving a beryllium secondary target coupled with an electron accelerator operated in the 4 to 9 MeV range with the utmost attention given the dubious reliability of the (γ, xn) cross-sections for ^{9}Be implemented in MCNP6.2.

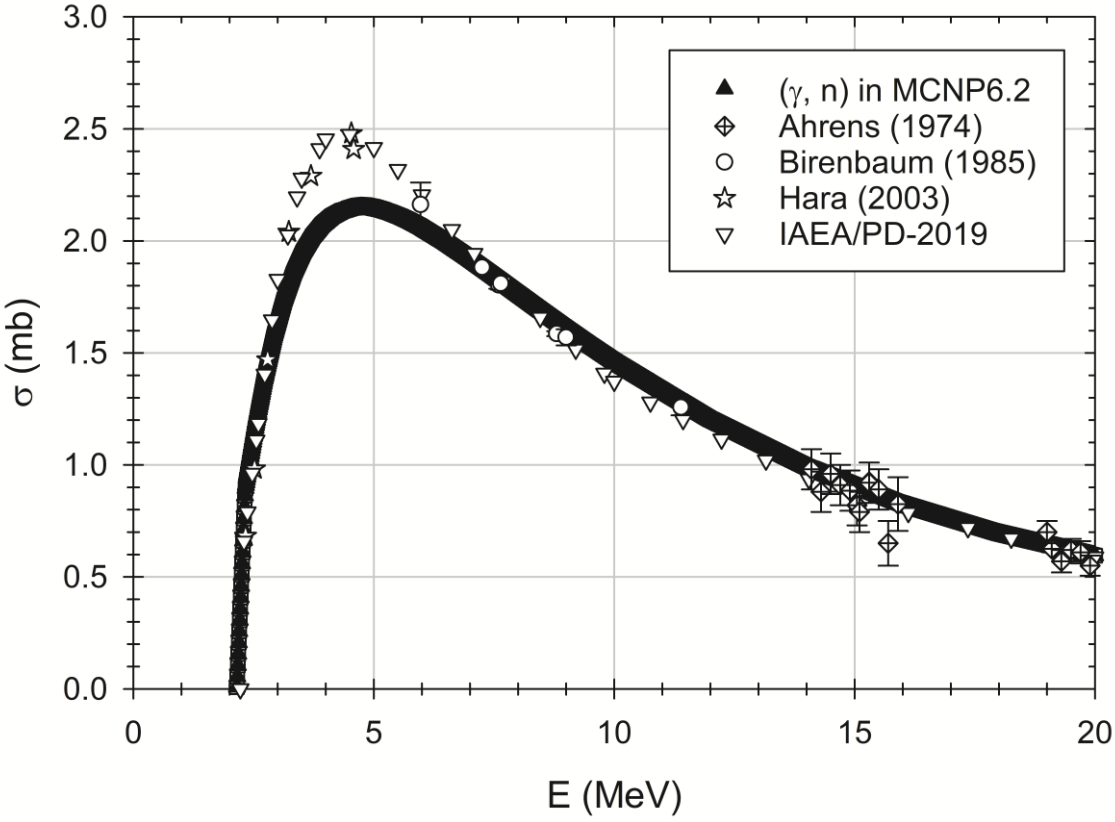

Fig. 16. Extraction of ^{2}H photonuclear cross-sections implemented in MCNP6.2 and comparison with experimental data.

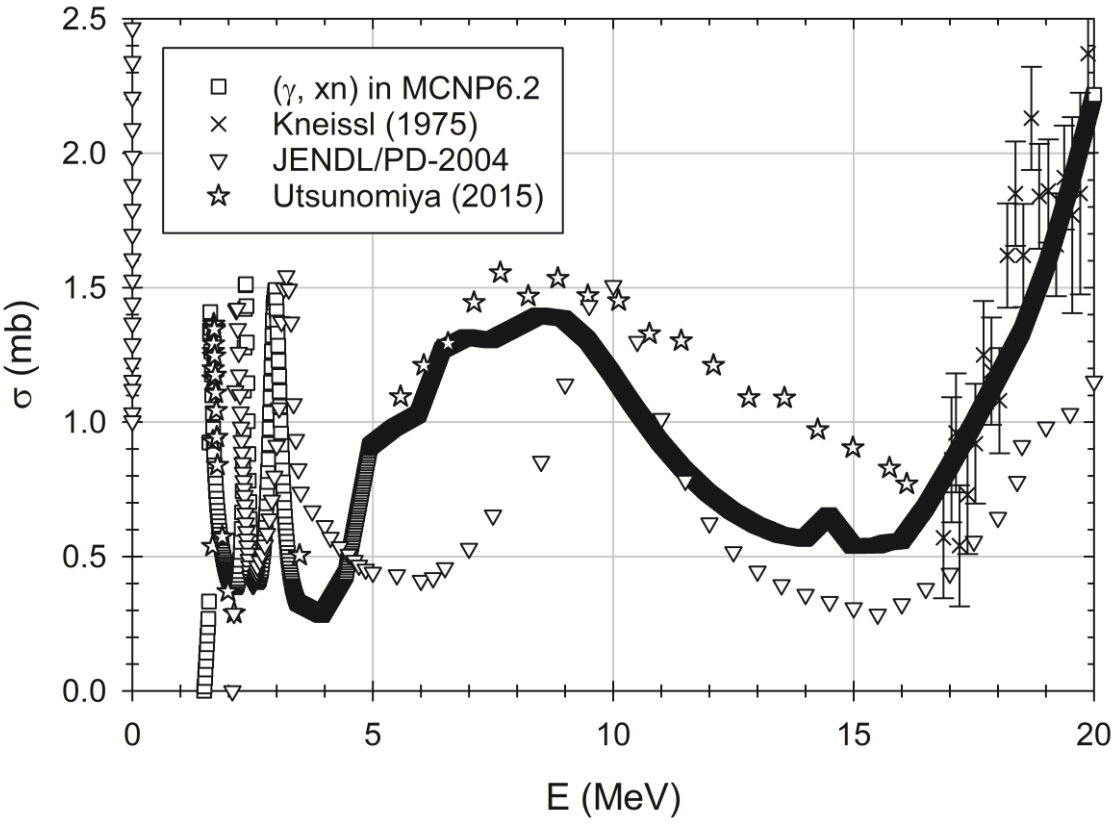

Fig. 17. Extraction of ^{9}Be photonuclear cross-sections implemented in MCNP6.2 and comparison with experimental data.

3.3.2 Energy distribution

We simulated with MCNP6.2 the energy distributions of the photoneutron fluxes emitted by both beryllium and heavy water secondary targets irradiated orthogonally by a 9 MeV photon beam (mono-energetic source). The secondary targets were simulated as 10 cm-diameter spheres. Fig. 18 presents the results obtained. The mean energy of the two spectra are respectively 2.6 and 3.5 MeV for the beryllium and heavy water targets. Fig. 19 shows the energy distributions of the photoneutron fluxes emitted by a heavy water secondary target irradiated by mono-energetic photons between 4 and 9 MeV by 1 MeV steps. The energy spectrum appears to be significantly harder when the photon energy increases. One would notice a certain number of dips in the energy spectra, for instance at 0.4, 1.0, 1.3, 1.65, 1.85 and 1.9 MeV. The latter are due to elastic scattering reactions of neutrons on ^{16}O contained in the heavy water target. To a lesser extent, (n, γ) reactions on ^{16}O may also occur and contribute marginally to the dips observed at around 0.4, 1.0, 1.65 and 1.85 MeV [17].

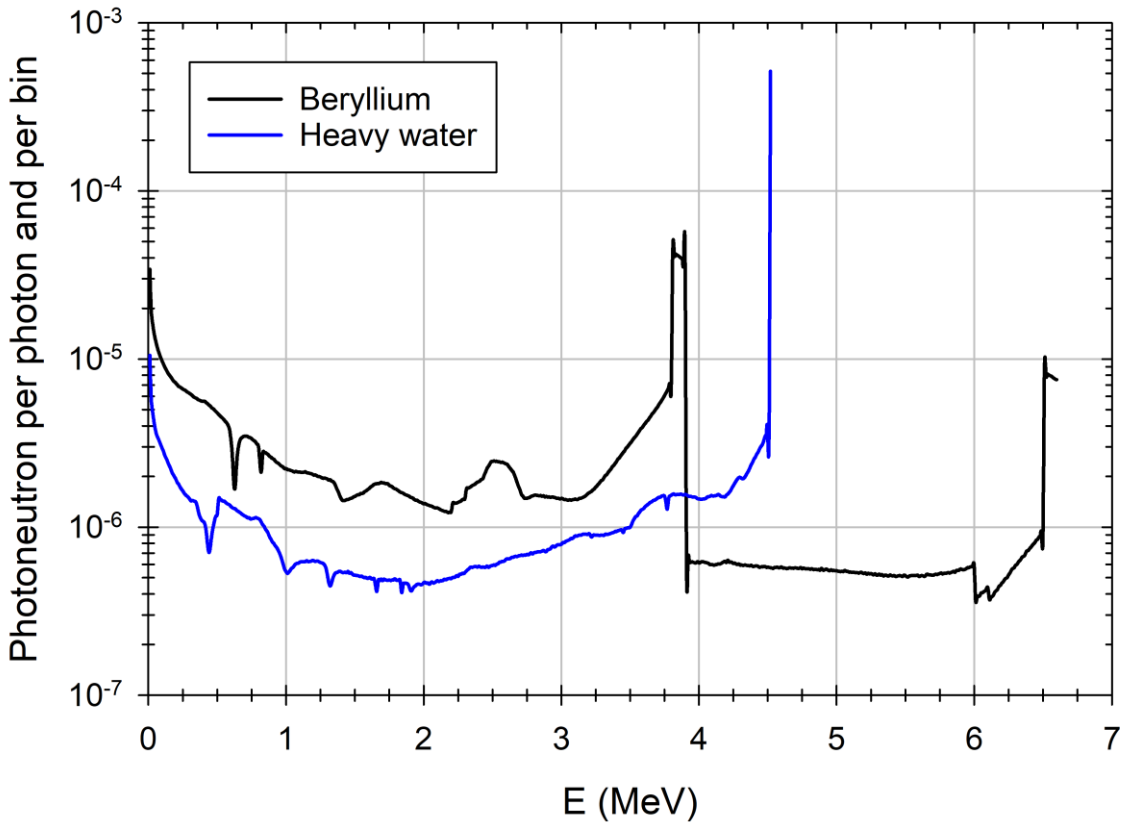

Fig. 18. Energy distributions of the photoneutron fluxes emitted by heavy water and beryllium secondary targets irradiated by 9 MeV mono-energetic photons, simulated with MCNP6.2.

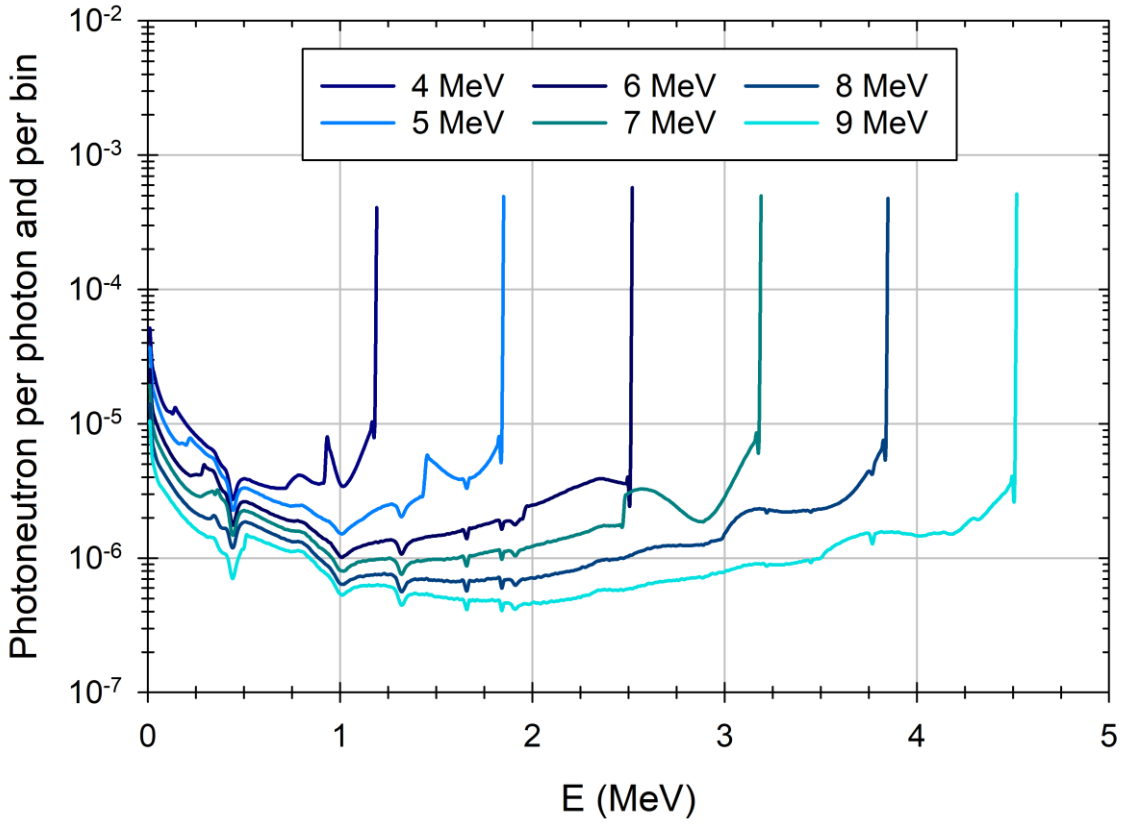

Fig. 19. Energy distributions of the photoneutron fluxes emitted by a heavy water secondary target irradiated by mono-energetic photons between 4 and 9 MeV by 1 MeV steps, simulated with MCNP6.2.

3.3.3 Angular distribution

We also simulated with MCNP6.2 the angular distributions of the photoneutron fluxes emitted by secondary targets irradiated orthogonally by mono-energetic photons between 4 and 9 MeV by 1 MeV steps. The secondary targets were once again simulated as 10 cm-diameter spheres. Fig. 20 presents the results obtained for a secondary target made of heavy water whereas Fig. 21 shows the results obtained for one made of beryllium, normalized distributions in all cases. The angular distribution of the photoneutron flux emitted by a heavy water secondary target appears to be peaked at 90° and the higher the photon energy the more this effect is pronounced. However, for the case of a beryllium secondary target, this effect is less marked but still noticeable for photon energies from 6 to 9 MeV. Fig. 22 presents the angular distributions of the components of the photoneutron flux from 0 to 5 MeV and from 5 to 20 MeV, emitted by a beryllium secondary target irradiated by 9 MeV mono-energetic photons. Both energy components appear to be peaked around 90°. Nevertheless, the most energetic component from 5 to 20 MeV is more strongly peaked at 90°.

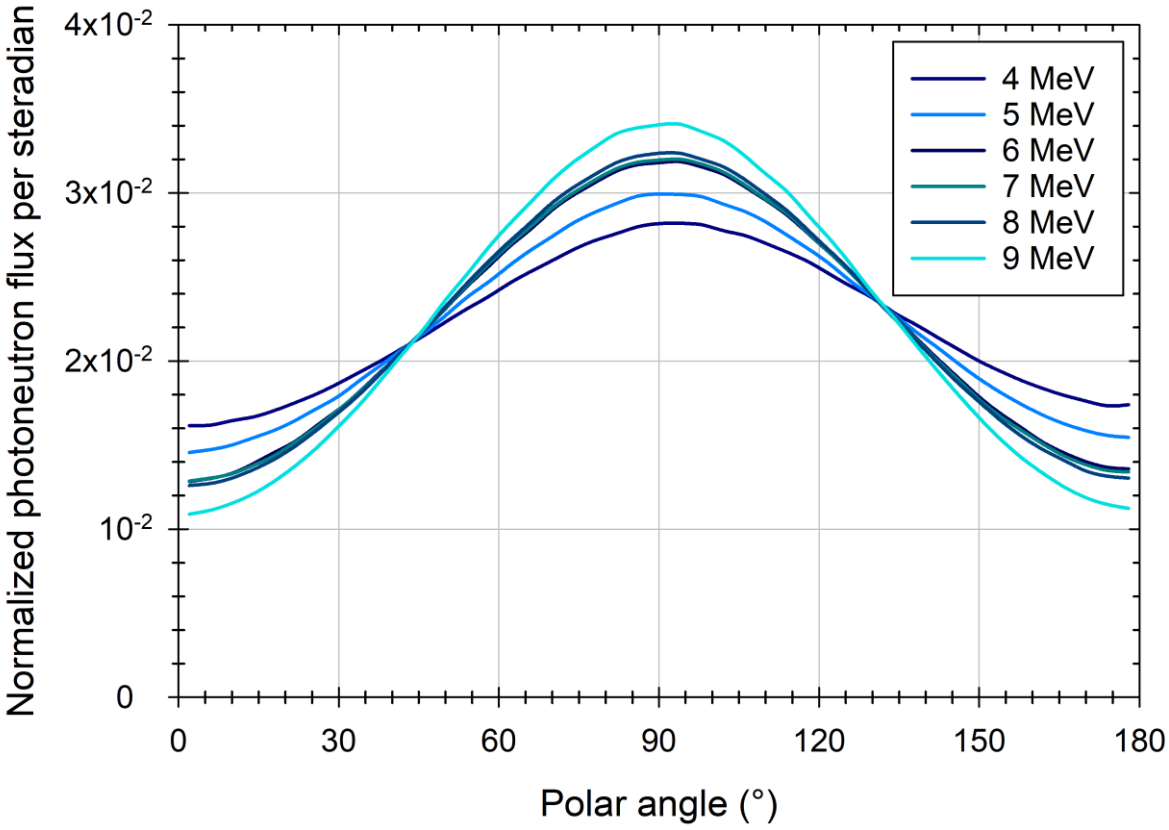

Fig. 20. Normalized angular distributions of the photoneutron fluxes emitted by a heavy water secondary target irradiated by mono-energetic photons between 4 and 9 MeV, simulated with MCNP6.2.

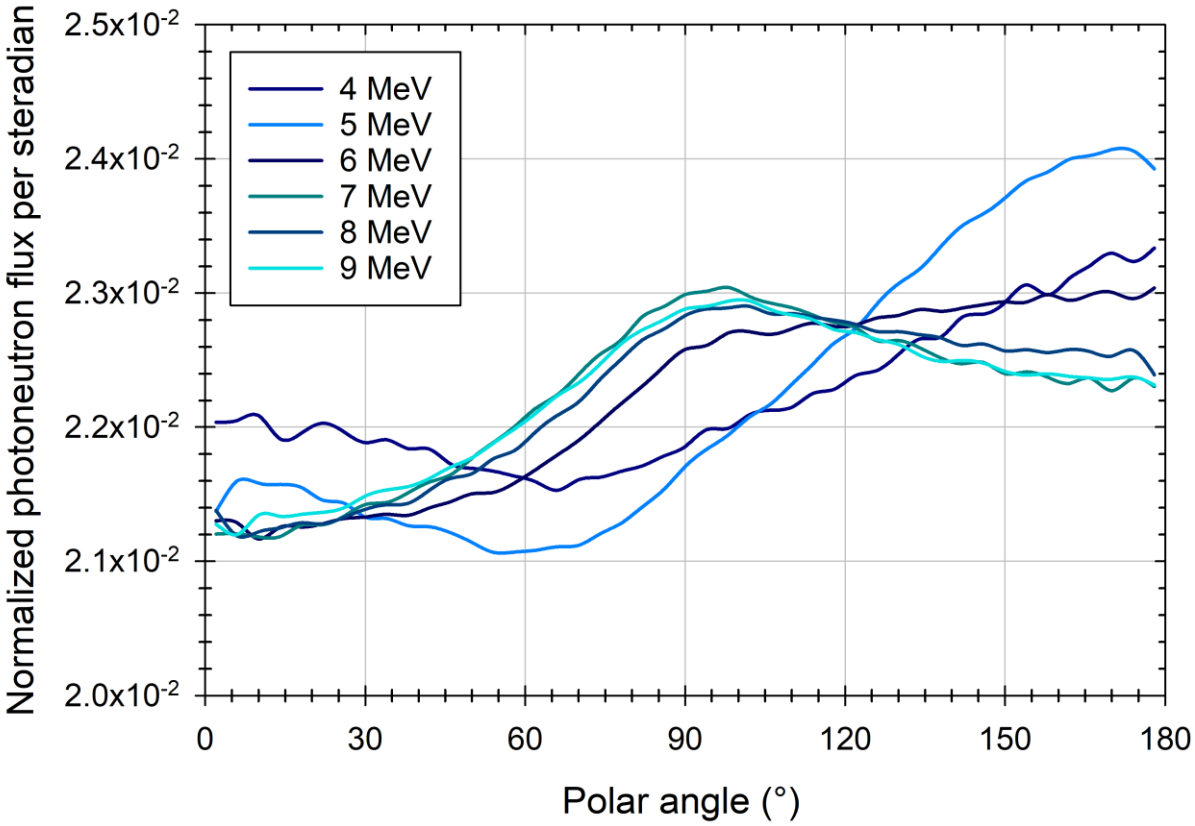

Fig. 21. Normalized angular distributions of the photoneutron fluxes emitted by a beryllium secondary target irradiated by mono-energetic photons between 4 and 9 MeV, simulated with MCNP6.2.

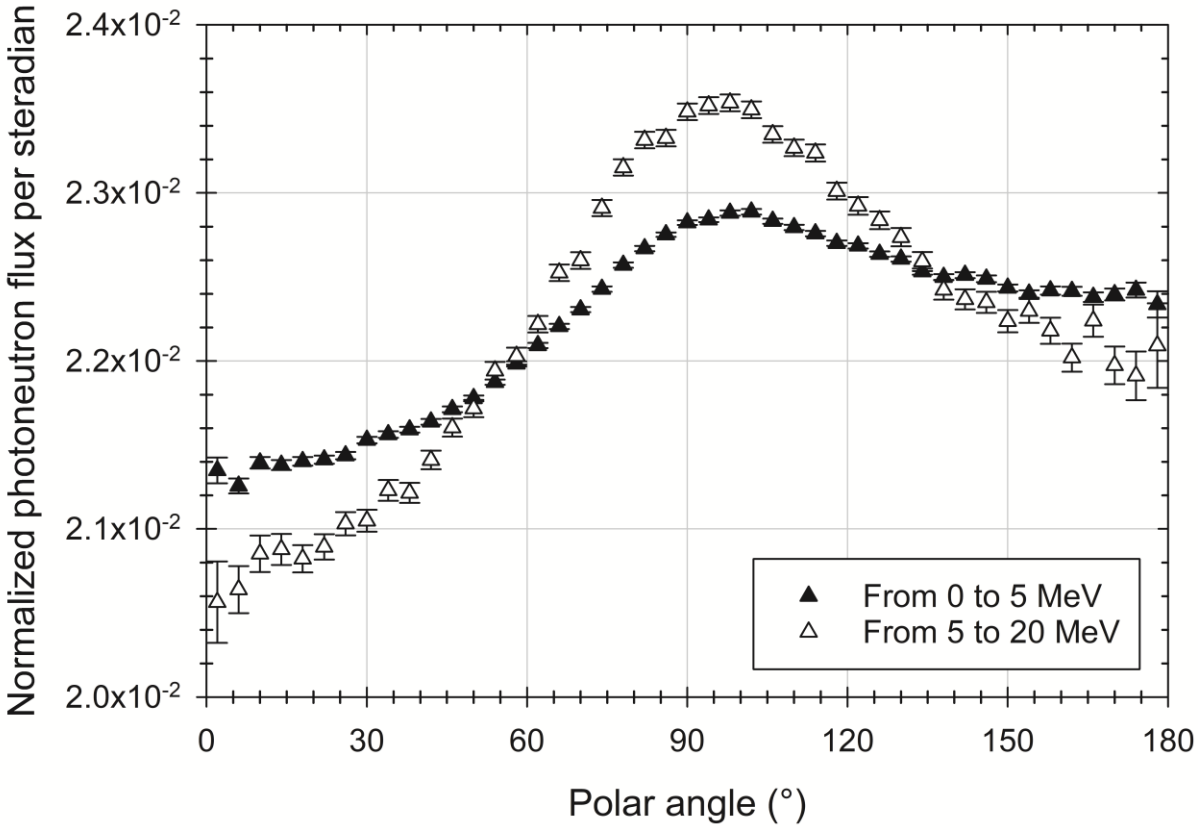

Fig. 22. Normalized angular distributions of the photoneutron flux components from 0 to 5 MeV and from 5 to 20 MeV, emitted by a beryllium secondary target irradiated by 9 MeV mono-energetic photons, simulated with MCNP6.2.

4. Monte Carlo simulation of photoneutron fluxes: benchmarking MCNP against neutron activation measurements

4.1 Materials and methods

In section 4, we will review the performance of the MCNP code to simulate photoneutron fluxes emitted by electron accelerators in the 4 to 20 MeV range. To evaluate the reliability of the characteristics of the photoneutron fluxes simulated with MCNP, the latter can be benchmarked against neutron activation measurements of vanadium and aluminium foils [32, 91]. The principle of the measurement is as follows. First, a foil is exposed to the photoneutron flux to measure its yield, leading to the activation of the foil, the production of measurable radioactive nuclei, which decay emitting gamma-rays of suitable energy and according to an appropriate half-life time. Then, the foil is positioned in front of a detector to acquire a gamma-ray spectrum and analyse the net peak area corresponding to the gamma of interest. To allow the comparison between the net peak areas simulated with the ones obtained experimentally, the net peak area is calculated with the following formula [17, 32, 91] valid for short-pulse irradiations,

$$\mathcal{A}_\gamma = R_{(n,\ \gamma)}\, I_\gamma\, \varepsilon_\gamma\, \frac{1 - e^{-n\lambda T}}{1 - e^{-\lambda T}}\, t_1\, e^{-\lambda t_2} \left(1 - e^{-\lambda t_3}\right)$$

With:

- $\mathcal{A}_\gamma$, the net peak area (in counts);
- $R_{(n,\ \gamma)}$, the $(n,\ \gamma)$ reaction rate in the vanadium or aluminum foil (number of reactions per second);
- I_γ, the emission intensity of the gamma-ray of interest (in %);
- ε_γ, the detection efficiency of the gamma detector;
- n, the number of pulses during the irradiation;
- λ, the decay constant of the radioactive nucleus (in seconds^{-1});
- T, the pulse period (in seconds);
- t_1, the pulse duration (in seconds);
- t_2, the cooling time (in seconds);

- t_3, the counting time (in seconds).

In this formula, the $(n,\ \gamma)$ reaction rate in the foil is calculated with the MCNP code using an *F4* tally coupled with an *FM4 card*. Other terms of the equation either depend on the experimental protocol or are extracted from nuclear databases [17, 32, 91].

4.2 Results

4.2.1 Photoneutron flux emitted by a tungsten or tantalum target

The benchmarking methodology presented in section 4.1 has been deployed on a Sagittaire accelerator (CEA Paris-Saclay, France) equipped with either a tungsten or tantalum target and operated at average electron energies of 14 or 17 MeV [32]. The vanadium or aluminium foils were positioned in a polyethylene box and surrounded by cadmium (see Figs. 1 and 2 from [32]), the whole constituting an activation detector. Table 3 gathers the results obtained using cross-sections for the (n, γ) reactions on ^{51}V and ^{27}Al from the ENDF/B-VI nuclear data library (the relative deviations between results obtained using (n, γ) cross-sections from ENDF/B-VI and ENDL-92 are within 8 and 18% [32]). Whatever the average electron energy, results obtained with the tungsten and the tantalum targets show similar trends. Indeed, calculations carried out took into account two energy-dependent correction factors to compensate the erroneous thresholds of the (γ, xn) cross-sections encountered with a tungsten target when using the MCNP code. At 14 MeV, the MCNP code underestimates experiment by roughly 40%. At 17 MeV, this underestimation reaches 50%, or in other words a factor of two. Moreover, additional measurements carried out with the Linatron M9 accelerator of the SAPHIR platform (CEA Paris-Saclay, France) equipped with a tungsten target and collimator (without any secondary target) and operated at an electron energy of 9 MeV suggest that for this material and at this energy the underestimation rises to a factor of the order of ten [91].

	14 MeV		17 MeV	
	Tungsten	Tantalum	Tungsten	Tantalum
V	0.56	0.56	0.52	0.51
Al	0.65	0.59	0.49	0.47
Mean value	*0.61*	*0.58*	*0.51*	*0.49*

Table 3. Ratio between simulation and experimental results, the Sagittaire accelerator of the SAPHIR platform (CEA Paris-Saclay, France) equipped with either a tungsten or tantalum target, and operated at average electron energies of 14 or 17 MeV [32].

4.2.2 Photoneutron flux emitted by a heavy water secondary target

The benchmarking methodology has also been deployed on the Linatron M9 accelerator of the SAPHIR platform (CEA Paris-Saclay, France) operated at electron energies of 6 or 9 MeV and equipped with a 16 kg-heavy water secondary target [91]. The vanadium or aluminium foils were positioned inside a neutron cell made of polyethylene, the design of which was detailed in [92] (see Figs. 7 and 8 from [91]). Table 4 summarizes the results obtained. At 6 MeV, the MCNP code underestimates experiment by a factor of two. At 9 MeV, this underestimation is around 26%.

	6 MeV	9 MeV
V	0.48	0.73
Al	0.51	0.75
Mean value	*0.50*	*0.74*

Table 4. Ratio between simulation and experimental results, the Linatron M9 accelerator of the SAPHIR platform (CEA Paris-Saclay, France) equipped with a heavy water secondary target, and operated at electron energies of 6 or 9 MeV [91].

4.2.3 Photoneutron flux emitted by a medical accelerator

Reference [32] reports that this benchmarking methodology has also been deployed on a Saturne 43F medical accelerator designed by General Electric (CEA Paris-Saclay, France) operated in photon mode at 12 or 20 MV accelerating voltages. Calculations were carried out using cross-sections for the (n, γ) reactions on ^{51}V and ^{27}Al from the ENDL-92 nuclear data library, which was released by the Lawrence Livermore National Laboratory (LLNL, USA). Table 5 gathers the results obtained with the activation detector irradiated in the photon field while containing either a vanadium or an aluminium foil. Due to low counting statistics, measurements conducted with an aluminium foil at 12 MV were not exploitable. At 12 MV, the MCNP code underestimates experiment by a factor of the order of ten. At 20 MV, this underestimation is around 20%.

	12 MV	20 MV
V	0.12	0.79
Al	-	0.83
Mean value	-	*0.81*

Table 5. Ratio between simulation and experimental results, a Saturne 43F medical accelerator (CEA Paris-Saclay, France) operated in photon mode at either 12 or 20 MV accelerating voltages and vanadium or aluminium foils irradiated in the photon field [32].

4.3 Discussion

Whatever the energy at which electron accelerators are operated in the 4 to 20 MeV range, photoneutron activation calculations based on Monte Carlo simulations conducted with the MCNP code underestimate the experimental results. At first sight, the yields of the photoneutron fluxes simulated with MCNP seem to be underestimated, assumption that we will further investigate in the following. Considering the M9 Linatron accelerator operated at 9 MeV, photoneutrons are produced by tungsten and the underestimation climbs to a decade. Obviously, the (γ, xn) cross-sections thresholds errors met with the MCNP code (see section 3.2.1) should explain at least part of this discrepancy. Nevertheless, when tungsten is the sole photoneutron-emitting material in the setup simulated, a correction factor may be used *a posteriori* to circumvent the (γ, xn) cross-sections thresholds errors in MCNP. However, even if such a correction factor is taken into account when simulating a tungsten target, MCNP simulation results keep underestimating the experimental data by a few tens of percent in the 10 to 20 MeV range and the discrepancies are the same that the target is made of tungsten or tantalum (see Table 3). Thus, one could consider comparing results obtained with another Monte Carlo simulation code.

A comparison study between the Monte Carlo codes TRIPOLI-4 version 9 [56] and MCNPX version 2.7.B [79] for the photoneutron yields of tungsten and tantalum targets irradiated by electrons in the 10 to 20 MeV range is reported in [30]. This study showed that the gaps between results obtained with these two codes is overall around 10%, the yields determined with TRIPOLI-4 being lower than the ones obtained with MCNP. Consequently, it is likely that the underestimation obtained in the frame of photoneutron activation calculations carried out with MCNP would become even larger using TRIPOLI-4. On the other hand, Y. S. Kim *et al.* [93] simulated the photoneutron yields from tungsten, tantalum, lead, rhenium and gold targets irradiated by 10 or 15 MeV electrons and compared results obtained with two codes, *i.e.* MCNPX [79] and GEANT4 [94-96] (see in particular table 2 from [93]). The discrepancies encountered between the two codes are diverse and uneven, starting as low as 6% and up to a factor of nearly three. The explanation put forward

by Y. S. Kim *et al.* to interpret these discrepancies is the lack of comprehensive understanding in physics of the photonuclear process and secondary photoneutrons [93].

In any case, the underestimation trend encountered with the MCNP code when simulating photoneutron activation measurements could be at least partially due to either or both of the following causes:

- Lack of fundamental knowledge of photonuclear cross-sections near the energy thresholds of the reactions;
- Undervaluation of the maximum of the photonuclear cross-sections curves (as previously and suspiciously shown for ^{184}W in Fig. 8 for instance).

By way of illustration regarding the first hypothesis, a difference exceeding 0.5 MeV was pointed out by Y.-O. Lee *et al.* at the energy threshold of the (γ, n) reaction for ^{181}Ta when comparing experimental data measured at Saclay (7.45±0.2 MeV) and Livermore (8.0 MeV) [97]. As a reminder, at 14 and 17 MeV, the underestimations met with the MCNP code when simulating neutron activation measurements are respectively around 40% and approximately at a factor of two for both tungsten and tantalum (see Table 3). Three important comments can be made. First, it is remarkable that the underestimation is higher at 17 than 14 MeV, which at least supports the second assumption. Second, if tungsten and tantalum photonuclear cross-sections are undervalued in the energy range of interest, the order of magnitude of this undervaluation seems to be rather similar for the two materials. Third, the underestimations obtained at 14 and 17 MeV initially reported in [32] are in good agreement with results obtained by K. Kosako *et al.* [66] who compared neutron activation calculations based on MCNP5 simulations and experiments using an electron accelerator operated at 18 MeV. Indeed, K. Kosako *et al.* showed that the calculations underestimate the measured data by a factor of 1.5 to 2.5 at 18 MeV. It is worth to notice that given these discrepancies, K. Kosako *et al.* concluded that the reevaluations of the photoneutron production cross-sections of copper and tungsten isotopes below 20 MeV are necessary in view of improving the calculation accuracy.

Regarding the photoneutron fluxes generated by medical accelerators, the photonuclear reactions mainly occur in the jaws, the primary collimator and the target. Due to the complex geometries of such accelerators, different materials like tungsten, lead, steel, etc., are often involved in the production of photoneutrons. For instance, the Saturne 43F medical accelerator emits photoneutrons through photonuclear reactions on both tungsten and lead, and the jaws of the accelerator emit about half of the photoneutron flux (see Table IV and Fig. 10 of [32]). Such diversity in terms of materials and neutron emitting elements renders non-trivial the application of a correction factor on simulation results during the post-processing step to compensate the (γ, xn) cross-sections threshold errors for tungsten in MCNP. Considering the Saturne 43F accelerator operated at 12 MV, the underestimation of the order of a factor of ten (see Table 5) could be explained at least by the cumulative effects of both (γ, xn) cross-section threshold errors for tungsten in the nuclear data from the MCNP code and questionable evaluations of (γ, xn) cross-sections for tungsten and lead.

When it comes to photoneutrons emitted by a heavy water secondary target, simulation of neutron activation measurements carried out using the version 6.1 of MCNP [98] underestimates experiment by a factor of two at 6 MeV and by 26% at 9 MeV (see Table 4). These discrepancies seem to show that the higher the electron energy, the more reliable is the photoneutron yield from the heavy water target simulated with the MCNP code. One could be tempted to use these values as scaling factors to reevaluate the photoneutron yields simulated with MCNP in a post-processing step. However, this approach would only be correct if the discrepancies found with MCNP are only and exclusively due to underestimations of the photoneutron yields, *i.e.* without any impact from the photoneutron energy spectrum on these discrepancies. Furthermore, a recent feasibility study in view of conducting linac-based neutron activation analysis to detect and quantify copper in scrap metal involved a 16 kg heavy water secondary target coupled with the Linatron M9 accelerator of the SAPHIR platform (CEA Paris-Saclay, France) operated at 6 MeV [17]. Using the version MCNP6.2 [36, 37] of MCNP, this study showed that simulation of neutron activation measurements of copper underestimate experiment roughly by a factor of two, which corroborates prior conclusions provided in [91] and according to which the the (γ, n) reaction cross-sections for deuterium are likely to be undervalued in the ENDF library.

It is worth to recall that in section 3.3.1, Fig. 16 illustrated a noticeable undervaluation of the (γ, n) reaction cross-sections for deuterium provided in ENDF. Nevertheless, algorithms used to simulate photoneutron production should also be carefully reexamined as some erroneous equations for photoneutron production can be found implemented in Monte-Carlo simulation codes, even in widely and commonly used ones such as MCNP [57].

D. A. Fynan reported that numerous works [99-107] introduce the Wattenberg or Hanson approximations to describe photoneutron kinematics but without discussion nor derivation [57]. Moreover, E. Caro found the photoneutron energy-angle relationship was modelled in MCNP5 [108] using *neutron inelastic scattering* equations [109], which leads to significant errors especially when the target nucleus is a light particle, *i.e.* deuterium. Regarding the MCNP code, whatever the version considered among which MCNP5 [108], MCNPX [79], MCNP6.1 [98], MCNP6.2 [36, 37], photoneutron kinematics modelling is not documented. We suspect that the same algorithms are used for photonuclear physics modelling in these different versions of the MCNP code, although slight differences can be found regarding the photonuclear data available. For instance, photonuclear cross-sections from CNDC are available in MCNPX but not in MCNP6. Anyway, the investigations carried out by E. Caro [109] and D. A. Fynan [57] enabled to identify with a high level of confidence the equations erroneously implemented in the MCNP code to model photoneutron kinematics (see Eqs. (30) and (32) from reference [57]). Inelastic neutron scattering equations are inappropriate to describe photoneutron kinematics, which leads to wrong and significantly hardened photoneutron energy spectra [57]. D. A Fynan suspects that discrepancies between simulation and experiment reported in [91] are dominated by spectral effects in the simulation data induced by the incorrect photoneutron kinematics modeling in the MCNP6 code. Nevertheless, inaccuracies of the photonuclear reaction cross-sections may also somehow contribute to the discrepancies encountered between MCNP simulation and experiment when dealing with photoneutrons emitted by an electron accelerator operated in the 4 to 20 MeV, in the context in which the reliability of photonuclear data has been openly discussed by V. V. Varlamov in 2019 [110].

5. Conclusions and recommendations

In this paper, we examined the performance of Monte Carlo codes to simulate photoneutron fluxes emitted by electron accelerators operating between 4 and 20 MeV. In this energy range and from a theoretical point of view, photoneutrons are created through the *giant dipole resonance* regime of the total photonuclear cross-section. These photoneutrons can be emitted by two different processes, each giving them specific properties:

- "boiled off photoneutrons" are emitted by *evaporation process*, and are characterized by lower energies and an isotropic emission;
- "knock-on photoneutrons" are emitted by *direct emission process*, and are characterized by higher energies and an anisotropic emission (in $\sin^2(\theta)$, *i.e.* with a privileged emission angle around 90° from the incident photon).

These fundamental characteristics enable to describe photoneutrons at the time of their creation and at the atomic nucleus scale. However, from a macroscopic point of view, several parameters of the electron accelerator influence the energy and angular distributions of the photoneutron fluxes generated, such as accelerator geometry, materials present and operating electron energy. This justifies the common practice of using Monte Carlo transport codes to characterize photoneutron fluxes emitted by electron accelerators.

On another note, photonuclear reactions are not the only reactions at the origin of neutron emission by electron accelerators in the 4 to 20 MeV range. According to the *equivalent photon approximation*, electrons can produce *virtual photons* leading to electronuclear reactions. Thus, electroneutrons can be produced simultaneously with photoneutrons. However, the literature is rather poor regarding the measurement of (e, n) or (e, e'n) reaction cross-sections. Nevertheless, many authors reported that the electroneutron yield cross-sections are about 137 times smaller than the photoneutron yield cross-sections. This ratio was originally stated in 1984 in the NCRP report No. 79 and unfortunately postulated without demonstration. In this work, we have shown that this value seems to be only appropriate in materials like tantalum or tungsten for an energy close to 18 MeV. Overall, the contamination of photoneutron fluxes by electroneutrons increases with

the accelerator's operating electron energy. We evaluated that the photoneutron fluxes emitted by tungsten or tantalum targets are likely to be polluted by electroneutrons with contamination levels ranging from approximately 0.01% at 10 MeV to 2% at 20 MeV. Furthermore, when coupling an electron accelerator equipped with a tungsten or tantalum target with a secondary target made of beryllium or heavy water, the production of electroneutrons is foreseen to be limited to the primary target. In other words, the production of electroneutrons in a beryllium or heavy water secondary target would be nil. Regarding the energy spectra and angular distributions of electroneutrons produced by electron accelerators in the energy range studied, and given the current lack of scientific knowledge on these parameters, we recommend in the meantime assuming that electroneutron fluxes are characterized by the same energy spectra and angular distributions as photoneutron fluxes. Even when electronuclear reactions are implemented in Monte Carlo transport codes like GEANT4 or FLUKA, we advise using the codes sparingly and with a high level of vigilance when simulating electroneutron fluxes. Fundamental knowledge on energy spectra and angular distributions, as well as validated electronuclear data and extensive Monte Carlo code benchmarking are all cruelly lacking to judge as reliable whatever they are simulation results concerning electroneutron production from electron accelerators.

Using the MCNP6.2 Monte Carlo code, we evaluated the characteristics of photoneutron fluxes emitted by electron accelerators operating between 4 and 20 MeV. First, we characterized photoneutron fluxes emitted by tungsten or tantalum targets irradiated by electrons in the 7 to 20 MeV range. Then, we characterized photoneutron fluxes emitted by heavy water or beryllium secondary targets coupled with electron accelerators operated in the 4 to 9 MeV range. The photoneutron fluxes were characterized according to three main parameters: the photoneutron yield cross-sections, energy and angular distributions. With astonishment, we showed that (γ, xn) cross-sections threshold errors present in MCNPX when using the ENDF library, discovered in 2012 for some tungsten isotopes, are unfortunately still relevant in 2022 for MCNP6.2. In particular, we demonstrate that erroneous parameters in the nuclear data of MCNP6.2 lead to (γ, xn) cross-section threshold errors for two tungsten isotopes, *i.e.* ^{182}W and ^{186}W, which leads to a global underestimation

of photoneutron production in tungsten. For calculations involving a tungsten target irradiated by electrons between 7 and 20 MeV, we determined new scaling factors valid with MCNP6.2 in order to circumvent these problems in the nuclear data of the code (see Table 2), and which can be reused by the reader. Furthermore, by taking an in-depth look at nuclear data libraries, we showed that photoneutron yield cross-sections are sometimes poorly evaluated below 20 MeV. Indeed, the case of ^{184}W is distinctive and would by the way provide additional evidence to support the undervaluation trend of MCNP simulation regarding photoneuton production by a tungsten target in the energy range of interest. We can also regret the absence of experimental data regarding (γ, xn) reaction cross-sections for ^{180}W and ^{183}W, which raises questions about the reliability of their evaluations. It should be recalled that tungsten is perhaps one of the most common photoneutron-producing material present in electron accelerators working in the 4 to 20 MeV range and thus concerns many Monte Carlo code users. On top of that, when (γ, xn) reaction cross-section threshold errors are absent in MCNP and experimental are available, as it is the case for ^{181}Ta for instance, it is legitimate to ask whether more than 50 year-old – single – experimental evaluations should be revaluated (and let's hope validated) or not. Furthermore, this study also showed that the photoneutron energy spectrum simulated for a tantalum target has a non-physical shape under 0.5 MeV, which is perhaps due to erroneous algorithms in MCNP for photoneutron energy calculations. Moreover, this study enabled to infer that the MCNP code does not simulate the direct component of photoneutron fluxes for tungsten or tantalum targets. Besides, while focusing on photoneutrons emitted by a heavy water secondary target and based on cross-sections measured by different authors, we brought to light that the maximum of the (γ, n) cross-sections curve around 4.5 MeV for deuterium is undervalued in ENDF. In other words, the photoneutron flux emitted by a heavy water target coupled with an electron accelerator operated in the 4 to 9 MeV range is likely to be underestimated when simulated with the MCNP code. Moreover, in light of strong discrepancies between (γ, n) cross-sections for ^{9}Be taken from different references, we recommend conducting MCNP simulations involving a beryllium secondary target coupled with an electron accelerator operated in the 4 to 9 MeV range with the utmost attention given the dubious reliability of the (γ, xn) cross-sections for ^{9}Be implemented in MCNP6.2.

In view of assessing the performance of the MCNP code for the simulation of photoneutron fluxes delivered by electron accelerators in the energy range studied, we benchmarked MCNP against neutron activation measurements conducted with three different electron accelerators, and discussed the results and discrepancies obtained by referring to several articles published in the literature. Whatever the energy at which electron accelerators are operated in the 4 to 20 MeV range, photoneutron activation calculations based on Monte Carlo simulations conducted with the MCNP code systematically underestimate the experimental results. We showed that the underestimation climbs to a decade for photoneutrons produced in tungsten with a 9 MeV electron accelerator. When tungsten is the sole photoneutron-emitting material in the setup simulated and when a correction factor is used *a posteriori* to circumvent the (γ, xn) cross-section threshold errors in MCNP, simulation results keep underestimating the experimental data by a few tens of percent in the 10 to 20 MeV range and the discrepancies are the same that the target is made of tungsten or tantalum. When it comes to photoneutrons emitted by a heavy water secondary target coupled with an electron accelerator operating between 4 and 9 MeV, simulation of neutron activation measurements carried with MCNP also underestimates experiment by a few tens of percent. For the case of medical accelerators, due to their complex geometries, the photonuclear reactions usually occur on different parts of the machine and on different materials (tungsten, lead, etc.), which renders non-trivial the application of a correction factor on simulation results during the post-processing step to compensate the (γ, xn) cross-section threshold errors for tungsten in MCNP. Operating a Saturne 43F medical accelerator at 12 MV, we showed that the underestimation of results when simulating neutron activation measurements are of the order of a factor of ten. Regarding the MCNP code, whatever the version considered, among which: MCNP5, MCNPX, MCNP6.1, MCNP6.2, photoneutron kinematics modelling is not documented. We suspect that the same algorithms are used for photonuclear physics modelling in these different versions of the MCNP code. Another point is that the latter provide all photonuclear data at least from the ENDF library although slight differences can be found between certain versions. For instance, photonuclear cross-sections from CNDC are available in MCNPX but not in MCNP6. Anyway, the investigations carried out by E. Caro in 2016 and D.

A. Fynan in 2020 enabled to identify with a high level of confidence the equations erroneously implemented in the MCNP code to model photoneutron physics. In fact, the MCNP code uses erroneous equations related to *inelastic neutron scattering* to describe photoneutron kinematics, which results in the overestimation of photoneutron energy and subsequently in significantly hardened photoneutron energy spectra. Consequently, because of the decrease of the (n, γ) cross-sections when the neutron energy increases, this spectrum-hardening effect would contribute to the underestimation of MCNP simulation results when simulating photoneutron activation measurements of vanadium or aluminum foils. However, inaccuracies of the photonuclear reaction cross-sections may also somehow exacerbate these discrepancies, in the context in which the reliability of photonuclear data has been openly discussed by V. V. Varlamov in 2019.

In summary, from the three main sources of errors leading to unreliable simulated photoneutron fluxes:

- incorrect implementation of certain nuclear data in Monte Carlo codes;
- invalid modeling of photonuclear physics in Monte Carlo codes;
- lack of fundamental knowledge of photoneutron yield cross-sections (both near the energy thresholds of the reactions and at the maximum of the cross-sections curves),

several recommendations can be made. But first, let's underline that all improvements foreseen regarding photoneutron simulation accuracy should be done keeping an eye on all of those three potential sources of errors. The continuous interest for photoneutrons from the accelerator community should convince Monte Carlo code development teams to seek to improve photonuclear and electronuclear physics modelling. Both nuclear data files and photonuclear kinematics algorithms should be checked and improved. Perhaps, taking into account the feedbacks from code users could help to achieve these tasks in the most efficient way. We can also encourage the developers to openly document and publish these upcoming improvements. The support of the experimental nuclear physics community could enable to re-evaluate photonuclear cross-sections and improve further nuclear data implemented in Monte Carlo codes, perhaps starting by working on the most common photoneutron-producing materials present in (or associated with) electron accelerators,

such as: tungsten, tantalum, lead, beryllium and deuterium. Regarding the community of Monte Carlo code users, we suggest to avoid blind trust in simulation results involving the production of photoneutrons by electron accelerators in the 4 to 20 MeV range. Taking a step back and use of critical thinking is advisable when simulating photoneutrons, and even more for the case of electroneutrons. In practice, to judge the reliability level of simulation results involving photoneutrons, crosschecking results with experiment could represent a solution of interest, and if not possible, comparing at least results obtained with other codes. As further improvements in modelling of photonuclear physics may take some time to reach a high level of reliability – and even more for the case of electronuclear physics – it is wise for users to focus in the meantime on, first, understanding and then, mastering the current weaknesses of the codes.

At last, considering the diversity of skills required, *i.e.* verification and correction or validation of photonuclear data in Monte Carlo codes, implementation of appropriate photonuclear physics algorithms, as well as the establishment of new photonuclear cross-section evaluations, the key to such progress in photoneutron simulation will certainly rely through international and collaborative work. In the meantime, benchmarking codes like MCNP6, TRIPOLI-4 and PHITS could potentially help to take another step forward with the objective of refining the validity domain of the different Monte Carlo transport codes when simulating photoneutron fluxes emitted by electron accelerators in the 4 to 20 MeV range.

Acknowledgments

The author is grateful to Dr. Frédérick Carrel for proofreading this paper and providing helpful comments.

References

[1] C. Ongaro, A. Zanini, U. Nastasi, J. Rodenas, G. Ottaviano, C. Manfredotti, Analysis of photoneutron spectra produced in medical accelerators, Phys Med Biol, 45 (2000) L55-L61.

[2] W.L. Huang, Q.F. Li, Y.Z. Lin, Calculation of photoneutrons produced in the targets of electron linear accelerators for radiography and radiotherapy applications, Nucl Instrum Meth B, 229 (2005) 339-347.

[3] W.M. Abou-Taleb, M.H. Hassan, E.A. El Mallah, S.M. Kotb, MCNP5 evaluation of photoneutron production from the Alexandria University 15 MV Elekta Precise medical LINAC, Appl. Radiat. Isot., 135 (2018) 184-191.

[4] A.H. Karimi, H. Brkic, D. Shahbazi-Gahrouei, S.B. Haghighi, I. Jabbari, Essential considerations for accurate evaluation of photoneutron contamination in Radiotherapy, Appl. Radiat. Isot., 145 (2019) 24-31.

[5] N. Rojas-Arias, L. Sajo-Bohus, J.O. Tolosa-Cetina, M.A. Sandoval-Garzon, S.A. Martinez-Ovalle, New target with low photoneutron yield for LINAC radiotherapy applications, Appl. Radiat. Isot., 162 (2020).

[6] J.L. Jones, W.Y. Yoon, D.R. Norman, K.J. Haskell, J.M. Zabriskie, S.M. Watson, J.W. Sterbentz, Photonuclear-based, nuclear material detection system for cargo containers, Nucl Instrum Meth B, 241 (2005) 770-776.

[7] A. Sari, F. Carrel, A. Grabowski, F. Laine, B. Espinosa, J.P. Poli, P. Sibczynski, I. Della-Rocca, M. Foster, A. Etile, O. Roig, S. Maitrejean, S. Rogerat, T. Berthelier, E. Gasser, M. Slegt, R. de Goede, J. Groeneveld, H. de Wilde, M. Heerschop, Deployment of the First Photofission Measurement System Dedicated to SNM Detection in Europe: Outcomes and Future Prospects, Ieee Nucl Sci Conf R, Manchester, United Kingdom, 2019, pp. 1-2.

[8] A. Lyoussi, J. Romeyer-Dherbey, F. Jallu, E. Payan, A. Buisson, G. Nurdin, J. Allano, Transuranic waste detection by photon interrogation and on-line delayed neutron counting, Nucl Instrum Meth B, 160 (2000) 280-289.

[9] M. Gmar, F. Jeanneau, F. Laine, H. Makil, B. Poumarede, F. Tola, Assessment of actinide mass embedded in large concrete waste packages by photon interrogation and photofission, Appl. Radiat. Isot., 63 (2005) 613-619.

[10] F. Carrel, M. Agelou, M. Gmar, F. Laine, B. Poumarede, B. Rattoni, Measurement of Plutonium in Large Concrete Radioactive Waste Packages by Photon Activation Analysis, Ieee T Nucl Sci, 57 (2010) 3687-3693.

[11] I. Meleshenkovskii, A. Elayeb, R. De Stefano, A. Sari, Feasibility study of the photofission technique for radiological characterization of 220-L concrete-lined nuclear waste drums using 7 or 9 MeV linacs, Nuclear Instruments and Methods in Physics Research Section A: Accelerators, Spectrometers, Detectors and Associated Equipment, 1029 (2022) 166422.

[12] I. Meleshenkovskii, T. Ogawa, A. Sari, F. Carrel, K. Boudergui, Optimization of a 9 MeV electron accelerator Bremsstrahlung flux for photofission-based assay techniques using PHITS and MCNP6 Monte Carlo codes, Nucl Instrum Meth B, 483 (2020) 5-14.

[13] L.A. Franks, J.L. Pigg, J.T. Caldwell, M.R. Cates, W.E. Kunz, B.W. Noel, D.A. Close, High-Sensitivity Transuranic Waste Assay by Simultaneous Photon and Thermal-Neutron Interrogation Using an Electron Linear-Accelerator, Nucl Instrum Methods, 193 (1982) 571-576.

[14] F. Jallu, A. Lyoussi, C. Passard, E. Payan, H. Recroix, G. Nurdin, A. Buisson, J. Allano, The simultaneous neutron and photon interrogation method for fissile and non-fissile element separation in radioactive waste drums, Nucl Instrum Meth B, 170 (2000) 489-500.

[15] A. Sari, F. Carrel, F. Laine, A. Lyoussi, Neutron interrogation of actinides with a 17 MeV electron accelerator and first results from photon and neutron interrogation non-simultaneous measurements combination, Nucl Instrum Meth B, 312 (2013) 30-35.

[16] A. Sari, S. Garti, F. Lainé, F. Carrel, J. Dumazert, H. Makil, N. Dufour, C. Mougel, A. Masset, L. Mondon, L. Boutillon, J.-P. Lejeune, The Potential of Photon Activation and Neutron Activation Techniques for Fast Soil Characterization, EPJ Web Conf., 225 (2020) 09001.

[17] A. Sari, S. Garti, F. Laine, H. Makil, N. Dufour, R. Woo, F. Carrel, P. Russo, Detection and quantification of copper in scrap metal by linac-based neutron activation analysis, Appl. Radiat. Isot., 166 (2020) 109339.

[18] R.L. Moss, Critical review, with an optimistic outlook, on Boron Neutron Capture Therapy (BNCT), Appl. Radiat. Isot., 88 (2014) 2-11.

[19] Y.S. D. A. Fynan, G. Kim, S. Barros, M. J. Kim, Photoneutron production in heavy water reactor fuel lattice from accelerator-driven bremsstrahlung, Ann Nucl Energy, 155 (2021).

[20] F. Carrel, B. Charbonnier, R. Coulon, F. Laine, S. Normand, C. Salmon, A. Sari, Characterization of Old Nuclear Waste Packages Coupling Photon Activation Analysis and Complementary Non-Destructive Techniques, Ieee T Nucl Sci, 61 (2014) 2137-2143.

[21] M.J. Berger, S.M. Seltzer, Bremsstrahlung and Photoneutrons from Thick Tungsten and Tantalum Targets, Phys Rev C, 2 (1970) 621-+.

[22] S.M. Seltzer, M.J. Berger, Photoneutron Production in Thick Targets, Phys Rev C, 7 (1973) 858-861.

[23] IAEA, Handbook on photonuclear data for applications: Cross sections and spectra, Vienna, Austria, 2000.

[24] L. Lakosi, C. Tam Nguyen, J. Bagi, Photoneutron interrogation of low-enriched uranium induced by bremsstrahlung from a 4MeV linac, Nuclear Instruments and Methods in Physics Research Section B: Beam Interactions with Materials and Atoms, 266 (2008) 295-300.

[25] L. Lakosi, C.T. Nguyen, Neutron interrogation of high-enriched uranium by a 4MeV linac, Nuclear Instruments and Methods in Physics Research Section B: Beam Interactions with Materials and Atoms, 266 (2008) 3295-3301.

[26] F. Jallu, A. Lyoussi, E. Payan, H. Recroix, A. Mariani, G. Nurdin, A. Buisson, J. Allano, Photoneutron production in tungsten, praseodymium, copper and beryllium by using high energy electron linear accelerator, Nucl Instrum Meth B, 155 (1999) 373-381.

[27] V.L. Chakhlov, Z.W. Bell, V.M. Golovkov, M.M. Shtein, Photoneutron source based on a compact 10MeV betatron1Work performed at the Institute of Introscopy, Tomsk Polytechnic University and at the Oak Ridge Y-12 Plant. The Oak Ridge Y-12 Plant is managed and operated by Lockheed Martin Energy Systems, Inc. for the US Department of Energy under contract DE-AC05-84OR21400.1, Nuclear Instruments and Methods in Physics Research Section A: Accelerators, Spectrometers, Detectors and Associated Equipment, 422 (1999) 5-9.

[28] K.M. Eshwarappa, G. Sanjeev, K. Siddappa, Y. Kashyap, A. Sinha, P.S. Sarkar, B.K. Godwal, Comparison of photoneutron yield from beryllium irradiated with bremsstrahlung radiation of different peak energy, Ann Nucl Energy, 34 (2007) 896-901.

[29] Y.G. Yang, Y.J. Li, H.D. Wang, T.Z. Li, B. Wu, Explosives detection using photoneutrons produced by X-rays, Nucl Instrum Meth A, 579 (2007) 400-403.

[30] A. Sari, F. Carrel, C. Jouanne, O. Petit, A. Lyoussi, Optimization of the photoneutron flux emitted by an electron accelerator for neutron interrogation applications using mcnpx and tripoli-4 monte carlo codes, 4th International Particle Accelerator Conference, IPAC 2013, Shanghai, China, 2013, pp. 3630-3632.

[31] A. Naseri, A. Mesbahi, A review on photoneutrons characteristics in radiation therapy with high-energy photon beams, Rep Pract Oncol Radiother, 15 (2010) 138-144.

[32] A. Sari, M. Agelou, I. Bessieres, F. Carrel, M. Gmar, F. Laine, A. Lyoussi, S. Normand, A. Ostrowsky, L. Sommier, Characterization of the Photoneutron Flux Emitted by an Electron Accelerator Using an Activation Detector, Ieee T Nucl Sci, 60 (2013) 693-700.

[33] NCRP Report No. 79, "Neutron Contamination from Medical Electron Accelerators: Recommendations of the National Council on Radiation Protection and Measurements", National Council on Radiation Protection and Measurements, Bethesda, MD (USA), 1984.

[34] G. Loi, M. Dominietto, I. Cannillo, M. Ciocca, M. Krengli, E. Mones, E. Negri, M. Brambilla, Neutron production from a mobile linear accelerator operating in electron mode for intraoperative radiation therapy, Phys Med Biol, 51 (2006) 695-702.

[35] M. Sohrabi, A. Hakimi, Novel 6MV X-ray photoneutron detection and dosimetry of medical accelerators, Physica Medica, 36 (2017) 103-109.

[36] C.J. Werner, MCNP Users Manual - Code Version 6.2, Los Alamos National Laboratory, 2017.

[37] C.J. Werner, MCNP6.2 Release Note, Los Alamos National Laboratory, 2018.

[38] J. Chadwick, M. Goldhaber, A 'Nuclear Photo-effect': Disintegration of the Diplon by γ-Rays, Nature, 134 (1934) 237.

[39] L.E.O. Szilard, T.A. Chalmers, Detection of Neutrons Liberated from Beryllium by Gamma Rays: a New Technique for Inducing Radioactivity, Nature, 134 (1934) 494-495.

[40] E.D. Courant, Direct Photodisintegration Processes in Nuclei, Phys Rev, 82 (1951) 703-709.

[41] D.J.S. Findlay, Applications of Photonuclear Reactions, Nucl Instrum Meth B, 50 (1990) 314-320.

[42] M. Goldhaber, E. Teller, On Nuclear Dipole Vibrations, Phys Rev, 74 (1948) 1046-1049.

[43] N. Bohr, J.A. Wheeler, The Mechanism of Nuclear Fission, Phys Rev, 56 (1939) 426-450.

[44] R.O. Haxby, W.E. Shoupp, W.E. Stephens, W.H. Wells, Photo-Fission of Uranium and Thorium, Phys Rev, 58 (1940) 92-92.

[45] W.P. Swanson, Radiological Safety Aspects of the Operation of Electron Linear Accelerators, IAEA, Vienna, 1979.

[46] V. Weisskopf, Statistics and Nuclear Reactions, Phys Rev, 52 (1937) 295-303.

[47] D.H. Wilkinson, Nuclear Photodisintegration, Physica, 22 (1956) 1039-1061.

[48] F. Tagliabue, J. Goldemberg, Angular Distributions of Fast Photoneutrons, Nucl Phys, 23 (1961) 144-152.

[49] G.S. Mutchler, The angular distributions and energy spectra of photoneutrons from heavy elements, Massachusetts Institute of Technology, 1966, pp. 308.

[50] J.M. Blatt, V.F. Weisskopf, Theoretical nuclear physics, Wiley, New York, 1952.

[51] G. Tosi, A. Torresin, S. Agosteo, A.F. Para, V. Sangiust, L. Zeni, M. Silari, Neutron Measurements around Medical Electron-Accelerators by Active and Passive Detection Techniques, Med Phys, 18 (1991) 54-60.

[52] R.F. Barrett, J.R. Birkelund, B.J. Thomas, K.S. Lam, H.H. Thies, Systematics of nuclear level density parameters of nuclei deficient in one neutron, Nuclear Physics A, 210 (1973) 355-379.

[53] T. von Egidy, D. Bucurescu, Systematics of nuclear level density parameters, Phys Rev C, 72 (2005).

[54] J.C. Liu, W.R. Nelson, K.R. Kase, X.S. Mao, Calculations of the giant-dipole-resonance photoneutrons using a coupled EGS4-morse code, United States, 1995, pp. 15.

[55] J.C. Liu, W.R. Nelson, K.R. Kase, X.S. Mao, Calculations of the Giant-Dipole-Resonance Photoneutrons Using a Coupled EGS4-Morse Code, Radiation Protection Dosimetry, 70 (1997) 49-54.

[56] O. Petit, N. Huot, C. Jouanne, Implementation of photonuclear reactions in the Monte Carlo transport code TRIPOLI-4 and its first validation in waste package field, Progress in Nuclear Science and Technology, 2 (2011) 798-802.

[57] D.A. Fynan, Photoneutron reaction kinematics and error of commonly used approximations, Nucl Instrum Meth A, 977 (2020) 164271.

[58] E. Fermi, Über die Theorie des Stoßes zwischen Atomen und elektrisch geladenen Teilchen, Zeitschrift fur Physik, 29 (1924) 315.

[59] C.F.v. Weizsäcker, Ausstrahlung bei Stößen sehr schneller Elektronen, Zeitschrift für Physik, 88 (1934) 612-625.

[60] E.J. Williams, Correlation of certain collision problems with radiation theory, Kong. Dan. Vid. Sel. Mat. Fys. Med., 13N4 (4) (1935) 1-50.

[61] M.N. Martins, E. Hayward, G. Lamaze, X.K. Maruyama, F.J. Schima, E. Wolynec, Experimental Test of the Bremsstrahlung Cross-Section, Phys Rev C, 30 (1984) 1855-1860.

[62] E. Wolynec, V.A. Serrao, M.N. Martins, Nuclear Size Effects in Virtual Photon Spectra, J Phys G Nucl Partic, 13 (1987) 515-526.

[63] M.I.C. Cataldi, E. Wolynec, M.N. Martins, P. Gouffon, Y. Miyao, Electrodisintegration of Pb-208, Bi-209 and Ta-181, J Phys G Nucl Partic, 14 (1988) 779-786.

[64] Y.Y. Yu, X.F. Weng, Y.Q. Yang, T.Y. Cui, Z.H. Zhang, S.R. Lin, Z. Zhang, Y.G. Yang, The study of fast neutrons production via the electrodisintegration reactions of high energy electrons, Nucl Instrum Meth A, 954 (2020).

[65] R. Bergere, H. Beil, A. Veyssiere, Photoneutron Cross Sections of La,Tb,Ho and Ta, Nuclear Physics A, A121 (1968) 463-+.

[66] K. Kosako, K. Oishi, T. Nakamura, M. Takada, K. Sato, T. Kamiyama, Y. Kiyanagi, Angular Distribution of Photoneutrons from Copper and Tungsten Targets Bombarded by 18, 28, and 38 MeV Electrons, J Nucl Sci Technol, 48 (2011) 227-236.

[67] V.M. Budnev, I.F. Ginzburg, G.V. Meledin, V.G. Serbo, The two-photon particle production mechanism. Physical problems. Applications. Equivalent photon approximation, Physics Reports, 15 (1975) 181-282.

[68] A. Tsechanski, D. Fedorchenko, V. Starovoitova, On the contribution of the electronuclear reaction to the photonuclear production of Mo-99 and other radioisotopes, Radiation Physics and Chemistry, 177 (2020) 109108.

[69] H.R. Vega-Carrillo, L.H. Pérez-Landeros, Electroneutrons around a 12 MV Linac, XIII International Symposium. XXIII National Congress on Solid State Dosimetry (ISSSD 2012), Ocoyoacac, Mexico, 2012.

[70] F. Biltekin, M. Yeginer, G. Ozyigit, Investigating in-field and out-of-field neutron contamination in high-energy medical linear accelerators based on the treatment factors of field size, depth, beam modifiers, and beam type, Phys Medica, 31 (2015) 517-523.

[71] T.G. Soto-Bernal, A. Baltazar-Raigosa, D. Medina-Castro, H.R. Vega-Carrillo, Neutron production during the interaction of monoenergetic electrons with a Tungsten foil in the radiotherapeutic energy range, Nucl Instrum Meth A, 868 (2017) 27-38.

[72] T.G. Soto-Bernal, A. Baltazar-Raigosa, D. Medina-Castro, H.R. Vega-Carrillo, Neutron production in the interaction of 12 and 18 MeV electrons with a scattering foil inside a simple LINAC head, Appl. Radiat. Isot., 139 (2018) 46-52.

[73] F. Mathew, G. Al Makdessi, L. Montgomery, M. Evans, J. Kildea, The impact of treatment parameter variation on secondary neutron spectra in high-energy electron beam radiotherapy, Phys Medica, 80 (2020) 125-133.

[74] V.T. Voronchev, V.I. Kukulin, B.M. Kuzhevskij, Electrodisintegration reaction in beryllium plasma as a source of neutrons, Nucl Instrum Meth A, 539 (2005) 640-645.

[75] M.B. Chadwick, M. Herman, P. Oblozinsky, M.E. Dunn, Y. Danon, A.C. Kahler, D.L. Smith, B. Pritychenko, G. Arbanas, R. Arcilla, R. Brewer, D.A. Brown, R. Capote, A.D. Carlson, Y.S. Cho, H. Derrien, K. Guber, G.M. Hale, S. Hoblit, S. Holloway, T.D. Johnson, T. Kawano, B.C. Kiedrowski, H. Kim, S. Kunieda, N.M. Larson, L. Leal, J.P. Lestone, R.C. Little, E.A. McCutchan, R.E. MacFarlane, M. MacInnes, C.M. Mattoon, R.D. McKnight, S.F. Mughabghab, G.P.A. Nobre, G. Palmiotti, A. Palumbo, M.T. Pigni, V.G. Pronyaev, R.O. Sayer, A.A. Sonzogni, N.C. Summers, P. Talou, I.J. Thompson, A. Trkov, R.L. Vogt, S.C. van der Marck, A. Wallner, M.C. White, D. Wiarda, P.C. Young, ENDF/B-VII.1 Nuclear Data for Science and Technology: Cross Sections, Covariances, Fission Product Yields and Decay Data, Nucl Data Sheets, 112 (2011) 2887-2996.

[76] A. Trkov, D.A. Brown, ENDF-6 Formats Manual: Data Formats and Procedures for the Evaluated Nuclear Data Files, United States, 2018, pp. Medium: ED; Size: 420 p.

[77] C.J. Werner, MCNP® User's Manual. Code Version 6.2, 2017.

[78] A. Sari, F. Carrel, M. Gmar, F. Laine, A. Lyoussi, S. Normand, Detection of Actinides With an Electron Accelerator by Active Photoneutron Interrogation Measurements, Ieee T Nucl Sci, 59 (2012) 605-611.

[79] E. D.B. Pelowitz, MCNPX Users Manual Version 2.7.0, 2011.

[80] A.M. Goryachev, G.N. Zalesnyy, Giant dipole resonance of W-182, 184, 186 isotopes and the shape of transitional nuclei with A= 170-198, Izv. Kaz. Akad. Nauk, Ser. Fiz.-Mat., 6 (1978).

[81] G.N.Z. A.M. Goryachev, S.F. Semenko, B.A. Tulupov, Giant Dipole Resonance in Nuclei of the Transitional Region Around A ≈ 190, Yad.Fiz., 17 (1973) 463.

[82] A. Veyssiere, H. Beil, R. Bergere, P. Carlos, A. Lepretre, A. Deminiac, Study of Giant Dipole Resonance in a=190 Transition Region, J Phys Lett-Paris, 36 (1975) L267-L270.

[83] B.L. Berman, M.A. Kelly, R.L. Bramblett, J.T. Caldwell, H.S. Davis, S.C. Fultz, Giant Resonance in Deformed Nuclei - Photoneutron Cross Sections for Eu153, Gd160, Ho165, and W186, Phys Rev, 185 (1969) 1576-+.

[84] J. Ahrens, H.B. Eppler, H. Gimm, M. Kröning, P. Riehn, H. Wäffler, A. Zieger, B. Ziegler, Photodisintegration of the deuteron at 15–25 MeV photon energy, Physics Letters B, 52 (1974) 49-50.

[85] Y. Birenbaum, S. Kahane, R. Moreh, Absolute cross section for the photodisintegration of deuterium, Phys Rev C Nucl Phys, 32 (1985) 1825-1829.

[86] K.Y. Hara, H. Utsunomiya, S. Goko, H. Akimune, T. Yamagata, M. Ohta, H. Toyokawa, K. Kudo, A. Uritani, Y. Shibata, Y.W. Lui, H. Ohgaki, Photodisintegration of deuterium and big bang nucleosynthesis, Physical Review D, 68 (2003) 072001.

[87] T. Kawano, Y.S. Cho, P. Dimitriou, D. Filipescu, N. Iwamoto, V. Plujko, X. Tao, H. Utsunomiya, V. Varlamov, R. Xu, R. Capote, I. Gheorghe, O. Gorbachenko, Y.L. Jin, T. Renstrøm, M. Sin, K. Stopani, Y. Tian, G.M. Tveten, J.M. Wang, T. Belgya, R. Firestone, S. Goriely, J. Kopecky, M. Krtička, R. Schwengner, S. Siem, M. Wiedeking, IAEA Photonuclear Data Library 2019, Nucl Data Sheets, 163 (2020) 109-162.

[88] U. Kneissl, G. Kuhl, K.H. Leister, A. Weller, Photoneutron Cross-Sections for Be-9 Obtained with Quasi-Monoenergetic Photons, Nuclear Physics A, 247 (1975) 91-102.

[89] H. Utsunomiya, S. Katayama, I. Gheorghe, S. Imai, H. Yamaguchi, D. Kahl, Y. Sakaguchi, T. Shima, K. Takahisa, S. Miyamoto, Photodisintegration of Be-9 through the 1/2(+) state and cluster dipole resonance, Phys Rev C, 92 (2015).

[90] N. Kishida, T. Murata, T. Asami, K. Kosako, K. Maki, H. Harada, Y.O. Lee, J.W. Chang, S. Chiba, T. Fukahori, JENDL photonuclear data file, Aip Conf Proc, 769 (2005) 199-202.

[91] A. Sari, F. Carrel, F. Laine, Characterization and Optimization of the Photoneutron Flux Emitted by a 6-or 9-MeV Electron Accelerator for Neutron Interrogation Measurements, Ieee T Nucl Sci, 65 (2018) 2539-2546.

[92] A. Sari, F. Carrel, F. Laine, A. Lyoussi, Design of a Neutron Interrogation Cell Based on an Electron Accelerator and Performance Assessment on 220 Liter Nuclear Waste Mock-Up Drums, Ieee T Nucl Sci, 61 (2014) 2144-2148.

[93] Y.S. Kim, Z. Khazaei, J. Ko, H. Afarideh, M. Ghergherehchi, Estimation of photoneutron yield in linear accelerator with different collimation systems by Geant4 and MCNPX simulation codes, Phys Med Biol, 61 (2016) 2762-2779.

[94] S. Agostinelli, J. Allison, K. Amako, J. Apostolakis, H. Araujo, P. Arce, M. Asai, D. Axen, S. Banerjee, G. Barrand, F. Behner, L. Bellagamba, J. Boudreau, L. Broglia, A. Brunengo, H. Burkhardt, S. Chauvie, J. Chuma, R. Chytracek, G. Cooperman, G. Cosmo, P. Degtyarenko, A. Dell'Acqua, G. Depaola, D. Dietrich, R. Enami, A. Feliciello, C. Ferguson, H. Fesefeldt, G. Folger, F. Foppiano, A. Forti, S. Garelli, S. Giani, R. Giannitrapani, D. Gibin, J.J.G. Cadenas, I. Gonzalez, G.G. Abril, G. Greeniaus, W. Greiner, V. Grichine, A. Grossheim, S. Guatelli, P. Gumplinger, R. Hamatsu, K. Hashimoto, H. Hasui, A. Heikkinen, A. Howard, V. Ivanchenko, A. Johnson, F.W. Jones, J. Kallenbach, N. Kanaya, M. Kawabata, Y. Kawabata, M. Kawaguti, S. Kelner, P. Kent, A. Kimura, T. Kodama, R. Kokoulin, M. Kossov, H. Kurashige, E. Lamanna, T. Lampen, V. Lara, V. Lefebure, F. Lei, M. Liendl, W. Lockman, F. Longo, S. Magni, M. Maire, E. Medernach, K. Minamimoto, P.M. de Freitas, Y. Morita, K. Murakami, M. Nagamatu, R. Nartallo, P. Nieminen, T. Nishimura, K. Ohtsubo, M. Okamura, S. O'Neale, Y. Oohata, K. Paech, J. Perl, A. Pfeiffer, M.G. Pia, F. Ranjard, A. Rybin, S. Sadilov, E. Di Salvo, G. Santin, T. Sasaki, N. Savvas, Y. Sawada, S. Scherer, S. Seil, V. Sirotenko, D. Smith, N. Starkov, H. Stoecker, J. Sulkimo, M. Takahata, S. Tanaka, E. Tcherniaev, E.S. Tehrani, M. Tropeano, P. Truscott, H. Uno, L. Urban, P. Urban, M. Verderi, A. Walkden, W. Wander, H. Weber, J.P. Wellisch, T. Wenaus, D.C. Williams, D. Wright, T. Yamada, H. Yoshida, D. Zschiesche, GEANT4-a simulation toolkit, Nucl Instrum Meth A, 506 (2003) 250-303.

[95] J. Allison, K. Amako, J. Apostolakis, H. Araujo, P.A. Dubois, M. Asai, G. Barrand, R. Capra, S. Chauvie, R. Chytracek, G.A.P. Cirrone, G. Cooperman, G. Cosmo, G. Cuttone, G.G. Daquino, M. Donszelmann, M. Dressel, G. Folger, F. Foppiano, J. Generowicz, V. Grichine, S. Guatelli, P. Gumplinger, A. Heikkinen, I. Hrivnacova, A. Howard, S. Incerti, V. Ivanchenko, T. Johnson, F. Jones, T. Koi, R. Kokoulin, M. Kossov, H. Kurashige, V. Lara, S. Larsson, F. Lei, O. Link, F. Longo, M. Maire, A. Mantero, B. Mascialino, I. McLaren, P.M. Lorenzo, K. Minamimoto, K. Murakami, P. Nieminen, L. Pandola, S. Parlati, L. Peralta, J. Perl, A. Pfeiffer, M.G. Pia, A. Ribon, P. Rodrigues, G. Russo, S. Sadilov, G. Santin, T. Sasaki, D. Smith, N. Starkov, S. Tanaka, E. Tcherniaev, B. Tome, A. Trindade, P. Truscott, L. Urban, M. Verderi, A. Walkden, J.P. Wellisch, D.C. Williams, D. Wright, H. Yoshida, Geant4 developments and applications, Ieee T Nucl Sci, 53 (2006) 270-278.

[96] J. Allison, K. Amako, J. Apostolakis, P. Arce, M. Asai, T. Aso, E. Bagli, A. Bagulya, S. Banerjee, G. Barrand, B.R. Beck, A.G. Bogdanov, D. Brandt, J.M.C. Brown, H. Burkhardt, P. Canal, D. Cano-Ott, S. Chauvie, K. Cho, G.A.P. Cirrone, G. Cooperman, M.A. Cortes-Giraldo, G. Cosmo, G. Cuttone, G. Depaola, L. Desorgher, X. Dong, A. Dotti, V.D. Elvira, G. Folger, Z. Francis, A. Galoyan, L. Garnier, M. Gayer, K.L. Genser, V.M. Grichine, S. Guatelli, P. Gueye, P. Gumplinger, A.S. Howard, I. Hrivnacova, S. Hwang, S. Incerti, A. Ivanchenko, V.N. Ivanchenko, F.W. Jones, S.Y. Jun, P. Kaitaniemi, N. Karakatsanis, M. Karamitrosi, M. Kelsey, A. Kimura, T. Koi, H. Kurashige, A. Lechner, S.B. Lee, F. Longo, M. Maire, D. Mancusi, A. Mantero, E. Mendoza, B. Morgan, K. Murakami, T. Nikitina, L. Pandola, P. Paprocki, J. Perl, I. Petrovic, M.G. Pia, W. Pokorski, J.M. Quesada, M. Raine, M.A. Reis, A. Ribon, A.R. Fira, F. Romano, G. Russo, G. Santin, T. Sasaki, D. Sawkey, J.I. Shin, I.I. Strakovsky, A. Taborda, S. Tanaka, B. Tome, T. Toshito, H.N. Tran, P.R. Truscott, L. Urban, V. Uzhinsky, J.M. Verbeke, M. Verderi, B.L. Wendt, H. Wenzel, D.H. Wright, D.M. Wright, T. Yamashita, J. Yarba, H. Yoshida, Recent developments in GEANT4, Nucl Instrum Meth A, 835 (2016) 186-225.

[97] Y.O. Lee, T. Fukahori, J. Chatt, Evaluation of photonuclear reaction data on tantalum-181 up to 140 MeV, J Nucl Sci Technol, 35 (1998) 685-691.

[98] T. Goorley, M. James, T. Booth, F. Brown, J. Bull, L.J. Cox, J. Durkee, J. Elson, M. Fensin, R.A. Forster, J. Hendricks, H.G. Hughes, R. Johns, B. Kiedrowski, R. Martz, S. Mashnik, G. McKinney, D. Pelowitz, R. Prael, J. Sweezy, L. Waters, T. Wilcox, T. Zukaitis, Initial Mcnp6 Release Overview, Nucl Technol, 180 (2012) 298-315.

[99] K. Mueck, F. Bensch, Emission-Spectra of Na-D2o, in-Be, La-Be and Na-Be Photoneutron Sources, J Nucl Energy, 27 (1973) 857-873.

[100] P.L. Reeder, R.A. Warner, Photoneutron energy spectra from 24Na□Be and 24Na□D, Nuclear Instruments and Methods, 180 (1981) 523-534.

[101] F.X. Gallmeier, General purpose photoneutron production in MCNP4A, United States, 1995, pp. Medium: ED; Size: 63 p.

[102] M. Watanabe, A. Yamamoto, Y. Yamane, Measuring the Photoneutrons Originating from D(gamma, n)H Reaction after the Shutdown of an Operational BWR, J Nucl Sci Technol, 46 (2009) 1099-1112.

[103] B.J. Patil, S.T. Chavan, S.N. Pethe, R. Krishnan, V.N. Bhoraskar, S.D. Dhole, Simulation of e-gamma-n targets by FLUKA and measurement of neutron flux at various angles for accelerator based neutron source, Ann Nucl Energy, 37 (2010) 1369-1377.

[104] F. Rahmani, M. Shahriari, Hybrid photoneutron source optimization for electron accelerator-based BNCT, Nucl Instrum Meth A, 618 (2010) 48-53.

[105] M. Tatari, A.H. Ranjbar, Design of a photoneutron source based on 10 MeV electrons of radiotherapy linac, Ann Nucl Energy, 63 (2014) 69-74.

[106] H.R. Vega-Carrillo, S.A. Martinez-Ovalle, Few groups neutron spectra, and dosimetric features, of isotopic neutron sources, Appl. Radiat. Isot., 117 (2016) 42-50.

[107] M.M. Rafiei, H. Tavakoli-Anbaran, Feasibility of using heavy water in order to design of a photoneutron source based on 5 MeV electron linear accelerator, J Instrum, 13 (2018).

[108] X.-M.C. Team, MCNP - Version 5, Vol. I: Overview and Theory, Los Alamos National Laboratory, 2003.

[109] E. Caro, Relativistic kinematics for photoneutron production in Monte Carlo transport calculations, Ann Nucl Energy, 96 (2016) 170-175.

[110] V.V. Varlamov, Reliability of Photonuclear Data: Various Experiments and Evaluations, Phys Part Nuclei+, 50 (2019) 637-643.